Thesis for the degree of Licentiate of Engineering

To fission or not to fission: ^{230}Ac

Anna Kawęcka

Department of Physics
Chalmers University of Technology
Gothenburg, Sweden 2024

To fission or not to fission: ^{230}Ac
Anna Kawęcka

Department of Physics
Chalmers University of Technology
SE-412 96 Gothenburg
Sweden
Telephone +46 (0)31-7721000

Cover: Constant excitation energy lines simulated for a solenoidal spectrometer. For a more detailed explanation, see caption of Fig. 4.4.

Chalmers Reproservice
Gothenburg, Sweden 2024

To fission or not to fission: ^{230}Ac

Anna Kawęcka
Department of Physics
Chalmers University of Technology

Abstract

Around half of the elements heavier than iron found in the Universe are believed to have been formed during the rapid neutron capture process (*r-process*). During the r-process, very neutron-rich nuclei are created through a series of neutron captures and β^--decay reactions. Eventually, the formed isotopes become so heavy that they can undergo nuclear fission. Thus, fission limits the mass of isotopes formed in the r-process. Fission probabilities and fission barrier heights of neutron-rich elements are essential inputs for r-process model calculations. However, studying the fission of these isotopes is extremely challenging due to the lack of available stable beam and target combinations that can result in the formation of interesting isotopes.

A novel technique employing a light-ion transfer reaction in inverse kinematics has been developed for obtaining fission data. As proven by a pilot experiment using a stable ^{238}U beam, the extraction of fission barrier heights using a (d,pf) reaction in inverse kinematics in a solenoidal spectrometer is possible, indicating promising future prospects.

This licentiate thesis focuses on improving the experimental approach used in the pilot experiment. In particular, the detection efficiency can be increased dramatically by using segmented silicon detectors covering a larger solid angle compared to the gas-filled detectors for fission fragments used in the pilot experiment. The new approach is more compact and allows also for the detection of γ-rays emitted from the fission fragments.

This development work was motivated by an upcoming experiment on the search for fission of ^{230}Ac using a radioactive ^{229}Ac beam. Importantly, this approach is versatile and can be applied to other isotopes of interest.

Keywords: Radioactive Beams, Fission, r-process, Heavy Elements, Actinides, CERN, ISOLDE, ISS

Acknowledgements

I would like to express my gratitude to my supervisor, Andreas Heinz, for all the work he has done to assist me in preparing this licentiate thesis and for answering my physics questions. I would also like to thank my co-supervisor, Thomas Nilsson, and my examiner, Christophe Demaziere, for their guidance and valuable suggestions. I am extremely grateful to Håkan Johansson, who provided me with very detailed comments on this thesis, on nuclear physics experiments in general, and introduced me to the world of data acquisition systems.

I want to thank Björn Jonson for the interesting physics talks, which are always inspiring. Special thanks to Hans Törnqvist for helping me with programming when issues arose. I appreciate being able to share this journey with a fellow PhD student, Maria Vittoria Managlia. Many interesting discussions arose during the conversation with the amanuens: Gabriel Ahlgren, Björn Johansson, Alfred Onbeck, Alice Svärdström, Isabella Tepp. I would like to thank Matthias Holl for help when simulation codes didn't want to cooperate. A huge thanks to the entire group for their support and for creating a warm atmosphere!

I would like to thank Katie Garrett, Ryan Tang and Ben Kay for carefully answering my questions about the ^{238}U(d,pf) experiment. Many thanks to the entire ISS collaboration for guidance and help, especially to Patrick MacGregor, David Sharp and Liam Gaffney.

Najważniejsze podziękowania chciałabym złożyć mojemu wspaniałemu mężowi, Wojtkowi. Dziękuję Ci, że zawsze mnie wspierasz i pomagasz przetrwać trudne chwile.

Contents

Chapter 1

Introduction

There are 118 known elements, 94 of which occur naturally on Earth.

The most mass-abundant element in the universe is hydrogen, making up around three-quarters of all matter. The remaining 25% is primarily composed of helium. The third-most abundant element is oxygen[1]. All other elements are generally uncommon.

Concerning the composition of the Earth, the situation is quite different. Elements making up the most mass of the Earth include oxygen (about 47%), silicon (28%), aluminum (8%), iron (5%), calcium (4%), sodium (3%), magnesium (2%), and potassium (2.5%). Additionally, heavier elements can be found on Earth, such as gold, platinum, uranium, thorium, and lead. A question arises — how were these elements formed?

The lightest elements — hydrogen, helium, and small trace amounts of lithium — were formed during the first minutes after the Big Bang through nuclear reactions in a process known as Big Bang Nucleosynthesis (BBN)[2].

[1] Stars burn hydrogen as their primary fuel source. Later in the lifetime of a star, after it has stopped burning hydrogen to helium, it transitions to burning helium to produce heavier elements. Massive stars undergo a catalytic cycle involving carbon, nitrogen, and oxygen, known as the CNO cycle. Lighter elements – lithium, beryllium, and boron – are not produced in stellar nucleosynthesis. However, in the later stages of the life of a star, helium burning leads to the formation of carbon, and the fusion of helium and carbon results in the production of oxygen. Consequently, nitrogen levels decrease, becoming somewhat less abundant, while oxygen is being produced, causing oxygen to become the third most abundant element in the Universe.

[2] In the BBN, only very few elements heavier than helium were produced because of a bottleneck: the absence of any stable nuclei with either 5 or 8 nucleons. Consequently, the production of heavier nuclei, including lithium-7, during this early cosmic phase was constrained. In stars, the bottleneck is overcome through triple-collisions of helium-4 nuclei, leading to the formation of carbon (the triple-alpha process). However, this process is slow and requires high densities, taking tens of thousands of years to convert a substantial amount of helium into carbon within stars. As a result, its contribution in the immediate minutes following the Big Bang was minimal.

Elements heavier than helium are created inside the cores of stars by fusion reactions. When light elements fuse, energy is released because the average binding energy per nucleon of the resulting nuclei is higher than that of the initial nuclei. Energy released by this process keeps the star from collapsing. The formed elements can be released into the surrounding galaxy by stellar explosions. However, elements heavier than iron and nickel cannot be formed in fusion reactions. As they are the most tightly bound nuclei, fusion of such elements no longer releases energy. Some light elements — lithium, beryllium, and boron — are thought to be formed in cosmic ray spallation, where they are remains from collisions of heavier elements with high-energy cosmic rays[3] [1].

Elements occurring naturally in the Solar System along with their astrophysical origin are presented in Fig. 1.1.

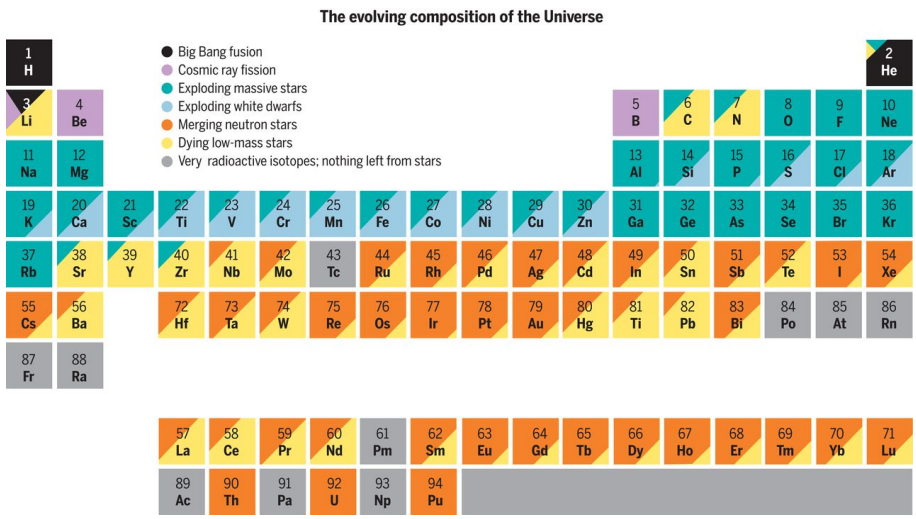

Figure 1.1: Elements occurring naturally in the Solar System and the astrophysical sources that are responsible for their creation. Figure from [2].

How elements heavier than iron are formed has been a mystery for many decades. In 1957, it was proposed that they are mainly synthesized by neutron-capture reactions [3, 4]. However, as the average half-life of free neutrons is about 10 minutes, neutron capture processes need to take place in specific astrophysical sites where sufficient fluxes of neutrons are available. The neutron capture reaction networks can be distinguished based on the neutron flux, and important for this licentiate thesis are the slow neutron capture (s) and rapid

[3]Cosmic rays mainly consist of protons and atomic nuclei (most of which are alpha particles).

neutron-capture (r) processes. The s-process only requires a low flux of neutrons. It is believed to occur mostly in the outer layers of Asymptotic Giant Branch[4] (AGB) stars. Neutrons for the s-process are supplied mainly by the $^{13}C(\alpha, n)^{16}O$ and $^{22}Ne(\alpha, n)^{25}Mg$ reactions, depending on the mass of the star[5] [5–7]. The s-process is a relatively slow process in which neutrons are caught one at a time, followed by β^--decay, forming isotopes along the line of β stability. The timescale of the s-process is between thousands to millions of years, typically with decades elapsing between successive neutron captures. The s-process can synthesise elements up to bismuth and it is believed that it has created around half of the elements heavier than iron in the universe. More information on the s-process can be found in Ref. [8].

Unlike the s-process, the r-process requires a high flux of free neutrons. The astrophysical site has been an open question for decades. Possible candidates proposed were neutron-star mergers and certain types of supernovae. The first strong observational evidence that a neutron star merger produces a neutron flux sufficient for the r-process was provided in 2017 through a multi-messenger observation of such a merger [9]. First, the gravitational-wave detectors LIGO and VIRGO detected a neutron star merger, GW170817 [10], which was followed by a kilonova[6] observation, AT2017gfo, in the electromagnetic spectrum ranging from radio- up to γ-frequency radiation. A neutron-capture element, strontium, was identified in the measured spectra. Strontium is one of the elements that can be produced through multiple neutron captures, and its isotopic composition and abundance patterns indicate that a neutron star merger can supply a neutron flux sufficient for the r-process [9].

During the r-process, several neutrons are captured sequentially through (n,γ) reactions, resulting in the formation of very neutron-rich isotopes. Eventually, the formed isotopes move sufficiently far from the line of β stability that β^- decay starts to compete with the capture of another neutron. After β^- decay, neutron capture is often again the next step. Neutron capture and β^- decay may also compete with photodissociation, i.e. (γ,n) reactions. The entire process is a complex reaction network extending across hundreds of neutron-rich isotopes far off the line of β stability. As the masses of the formed isotopes

[4] An AGB star, short for Asymptotic Giant Branch star, is a type of evolved star that is in a late stage of stellar evolution. These stars, usually ranging from low to intermediate mass (approximately 0.6 to 10 times that of the Sun), have exhausted the hydrogen in their cores and have entered the late phases of their lives.

[5] The $^{13}C(\alpha, n)^{16}O$ reaction takes place at temperatures around 100 MK, while the $^{22}Ne(\alpha, n)^{25}Mg$ reaction happens only if the temperature reaches above $\simeq$ 300 MK. In AGB stars with masses less than 4–5 Solar masses the temperature hardly reaches 300 MK so only the first reaction can take place [5].

[6] A kilonova is a transient astronomical event that occurs when two objects in a binary system, such as two neutron stars or a neutron star and a black hole, merge, resulting in a strong release of electromagnetic radiation. The term *kilonova* characterizes the peak brightness that reaches about 1000 times (*kilo*) that of a classical nova.

increase, at some point they become so heavy that nuclear fission becomes a possible decay channel. Thus, fission plays a crucial role insofar as it limits the mass of isotopes formed in the r-process.

Understanding the contribution of the r-process to the Solar System abundances is challenging because most of the isotopes involved in this process are very neutron-rich, thus far away from the β stability line. It is, in most cases, presently not possible to produce and study such isotopes in the laboratory. There is much more information available on the isotopes participating in the s-process[7], and traditionally the r-process abundances have been inferred by first fitting the calculated s-process abundance distributions to the total isotopic abundances measured in meteorites and attributing the remaining portion to the r-process [11]. The isotopic abundances in the solar system, separated into components from the r-process and s-process, are presented in Fig. 1.2. Elements primarily formed by the r-process include gold, platinum, and some rare-earth elements (like europium and gadolinium).

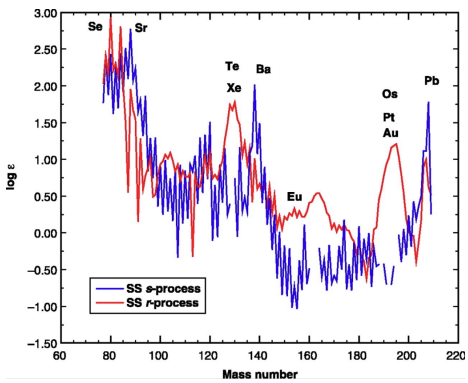

Figure 1.2: The solar system (SS) isotopic abundances, separated into components from the r-process and s-process. The s-process abundances are determined from the composition of solar meteorites. The observed abundances of elements in the mass region of gold and platinum, rare-earth elements, and tellurium and xenon cannot be explained without invoking the r-process. Figure from Ref. [11].

As mentioned earlier, the r-process involves a complex network of reactions with hundreds of isotopes. Some nuclear properties of isotopes involved in these reactions significantly influence the entire process of creating heavy elements in the universe, such as β-decay rates and nuclear masses of the participating isotopes. However, the r-process is ultimately limited once fission becomes

[7]Isotopes involved in the s-process are more stable, making them easier to produce and study.

possible. Then, a nucleus splits into two smaller fragments.

This makes fission, which effectively constrains the mass of isotopes formed by the r-process, to be of particular importance to understand this process. Moreover, the two fission fragments can subsequently capture additional neutrons, broadening the range of nuclei involved in the r-process. Thus, more information on fission of isotopes along the path of the r-process is essential for a deeper understanding of the formation of heavy elements.

1.1 Fission of neutron-rich nuclei

One of the key ingredients for r-process model calculations are the fission barriers and fission probabilities of the heavy r-process isotopes. The fission barrier refers to the energy barrier that prevents a nucleus from splitting into two fission fragments. However, as mentioned before, neutron-rich nuclei are very challenging to produce and study in the laboratory, which is the reason why the fission barriers of such isotopes are not known.

There are two ways for fission to happen: spontaneous fission (SF), and compound nucleus fission. SF plays a role for nuclei heavier than the nuclei which are the focus of this work. Here, we rather focus on the second alternative — the formation of a compound nucleus. One possibility to populate such a state is neutron-induced fission, where a target made of stable nuclei is bombarded with neutrons. Another option is fission induced by Light Charged Particles (LCPs), where light particles like protons or alpha particles impinge on a target. Fission can also be induced by bombarding a target with high-energy photons (real or virtual). Heavy-ion-induced fission, using multi-nucleon transfer reactions or fusion-fission reactions, allows for reaching elements further away from the β stability line than otherwise accessible. Exploring beta-delayed fission enables the study of unstable nuclei, when β-decay leads to the population of excited states in the daughter nucleus that are situated at excitation energies above the fission barrier. For heavy nuclei (such as actinides and transactinides), spontaneous fission can be observed. However, to study unstable nuclei, these methods are often not applicable due to the lack of appropriate target and beam combinations due to the overall shape of the β-stability line.

To get as close as possible to the r-process in the laboratory, one would need to use a target made of an element that is already quite rich in neutrons, bombard it with neutrons, and observe at which neutron energy fission becomes possible. Unfortunately, there are no stable targets that allow us to study isotopes directly interesting in terms of the r-process, and the available neutron fluxes are not high enough[8].

[8]It is worth mentioning that attempts have been made to produce heavy nuclei by bombarding target material with neutrons. However, due to limitations in available neutron fluxes, it has only been possible to synthesize elements up to fermium with an atomic number

This problem can be circumvented by using inverse kinematics. In inverse kinematics, a target made of a light, stable element is bombarded with a heavy beam, which can be unstable. As it currently is not possible to produce a target made of neutrons, a different approach is required. One such approach involves the use of surrogate reactions, for example a (d,p) reaction. In the (d,p) reaction, a heavy beam impinges on a deuteron. A neutron from the deuteron is transferred to the incident beam nucleus, whereas the proton is ejected from the target. The excitation energy of the formed nucleus can be extracted using the measured energy of the ejectile (proton in case of the (d,p) reaction). In this way, it is possible to study neutron-rich nuclei and their fission barrier.

In the inverse kinematics regime, the center of mass of the reaction has a significant velocity in the laboratory frame, which is nearly that of the beam. In direct kinematics (when a light beam impinges on heavy target) that is not the case — the velocity of the center of mass is small. Consequently, in inverse kinematics, the energy of the emitted ejectile becomes highly angle-dependent at backward angles in the laboratory frame[9], the separation between excited states in the laboratory frame is smaller than in the center of mass frame. This effect is known as kinematic compression [12] and impairs experimental resolution. It has been demonstrated that it is possible to mitigate this effect by using a solenoidal spectrometer [13]. The presence of a magnetic field separates reaction products spatially and eliminates kinematic compression. Moreover, in inverse kinematics, the fission fragments that always move in the forward direction have a lot of kinetic energy, which makes their detection easier.

1.1.1 Outline of the thesis

This licentiate thesis focuses on fission studies of neutron-rich nuclei using the (d,p) reaction in a solenoidal field. Chapter 2 introduces the kinematics of transfer reactions in a solenoidal field. Calibration and data analysis of a proof-of-principle ^{238}U(d,p) experiment with a stable beam, performed in 2021 at the Helical Orbit Spectrometer (HELIOS) in Argonne National Laboratory, are presented in Ch. 3. Finally, in Ch. 4, the preparations for fission studies with radioactive nuclei are presented using the example of a proposed and accepted (IS739) ^{230}Ac(d,pf) experiment at the ISOLDE Solenoidal Spectrometer (ISS) at ISOLDE, CERN.

$Z = 100$. Fermium was initially identified during the first test of a hydrogen bomb, but since this information was classified, researchers had to rediscover it using alternative methods.

[9]Many ejectile protons actually move in the forward direction. However, focusing on the measurement of protons emitted in backward angles in the laboratory, the ambiguity of some other reaction products is avoided since ejectiles equal or heavier than the target cannot be emitted backwards, unless the reaction has a large Q-value.

Author's contribution

Some parts of this work were produced with the assistance of other members of the group. The derivation of the transfer reaction kinematics in a magnetic field presented in Chapter 2 was a collaborative effort between the author of this licentiate thesis and another PhD student from the group.

Chapter 4 describes simulations and plans for the future ^{229}Ac(d,pf) experiment. It should be emphasized that the primary work of the author of this thesis presented in this chapter focused on gamma detector simulations. The author also contributed to the design of the detection system, particularly in calculating the efficiency of the luminosity detector described as the "standard ISS configuration", calculating the optimal position of the silicon array, and participated in the work on other elements presented in the thesis, but not as the primary executor.

The author of this thesis participated in several experiments at ISOLDE, CERN, (IS659, IS677, IS710, IS686, IS587, IS727), and a fusion-fission experiment at INFN Legnaro taking shifts, and working on the setup. Moreover, the author is also involved in testing digital data acquisition modules and development of the data acquisition system planned to be used for the ^{229}Ac(d,pf) experiment.

Chapter 2

Transfer reaction studies in a solenoidal field

We would like to study the fission of neutron-rich nuclei using the (d,p) reaction in inverse kinematics (IK) in a solenoidal field. This reaction is schematically shown in Fig. 2.1. A heavy projectile impinges on a deuteron[1]. During the interaction, a neutron from the deuteron is transferred to the heavy incident nucleus, whereas the remaining proton is ejected. The formed compound nucleus moves in the forward direction, is very likely excited, and may undergo fission, emitting two fission fragments and possibly neutrons and γ rays.

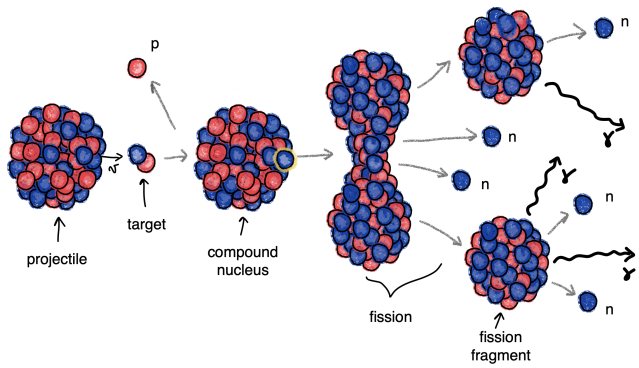

Figure 2.1: Schematic representation of the (d,p) reaction in inverse kinematics. A heavy projectile collides with the target (deuteron). During the interaction, a neutron (shown as blue) is transferred to the incident nucleus, and a proton (red) is ejected from the target. The formed compound nucleus moves in the forward direction and may undergo fission.

[1]Typically, solid deuterated polyethylene (CD_2) targets are used.

As mentioned before, the use of a magnetic field allows for better separation of the formed reaction products, thus improving the resolution of measurements. There are currently three solenoidal spectromters suited for this kind of experiments: the Helical Orbit Spectrometer (HELIOS) at Argonne National Laboratory (ANL), the SOLenoid spectrometer Apparatus for ReactIon Studies (SOLARIS) at FRIB, and the Isolde Solenoidal Spectrometer (ISS) at CERN. The design of ISS was inspired by HELIOS, shown in Fig. 2.2, thus their layouts are very similar. The beam enters the superconducting large-bore solenoid (with a 92.5 cm diameter) and travels through a hollow silicon array up to a deuterated polyethylene target (CD_2), where the (d,p) reaction can occur. If emitted in the (laboratory) backwards direction, the protons can then be detected in the silicon array, while the fission fragments can be detected with dedicated fission fragment detectors. As will be demonstrated, by measuring the energy and hit-position of the protons along the silicon array, it is possible to calculate the excitation energy of the compound nucleus formed in the transfer reaction. What is important to mention, in experiments of this kind, the beam energy is constant but nuclei with different excitation energy are populated. This allows to study a whole range of excitation energies.

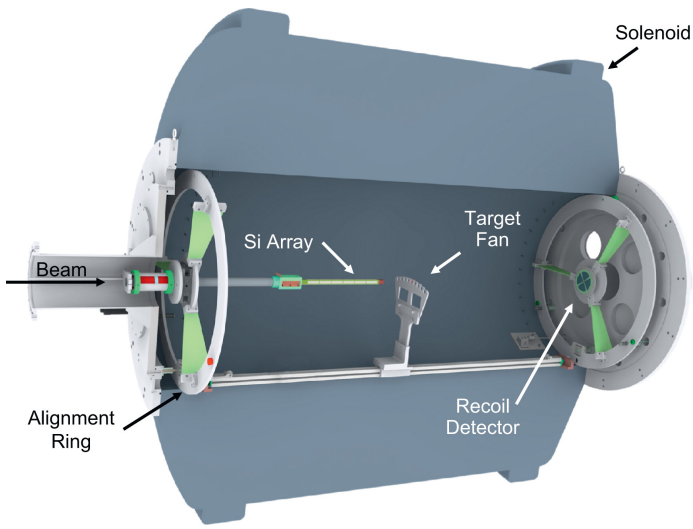

Figure 2.2: Schematic layout of HELIOS. The beam enters the superconducting large-bore solenoid magnet (92.5 cm diameter), travels through a hollow silicon array up to a target (CD_2), where the (d,p) reaction can occur. Figure from Ref. [13].

In this chapter, the kinematics of transfer reaction products in a solenoidal field will be described. We will begin with the straightforward case of a sta-

tionary charged particle source and then progress to a moving source. The equations will be derived in the relativistic kinematics regime. Following that, a step-by-step procedure for calculating the excitation energy of the compound nucleus and the emission angle of the ejected proton using information about the z-coordinate and the energy E deposited by the proton detected in the HELIOS/ISS spectrometer will be outlined. The derivation is based on Refs. [13–15].

After completing this chapter, the reader will understand the origin of the figure featured on the cover.

2.1 Stationary source

A particle of mass m and charge Z in a uniform magnetic field of strength B performs a helical motion with radius ρ given by

$$\rho = \frac{p_{xy}}{cZB} = \frac{mv_{xy}}{cZB}, \tag{2.1}$$

where p_{xy} is the momentum perpendicular to the magnetic field (in MeV/c unit), v_{xy} is the velocity perpendicular to the magnetic field, and c is the speed of light. The radius does not depend on the longitudinal velocity v_z. The time for one cycle (cyclotron period) is given by

$$T_{\mathrm{cyc}} = \frac{2\pi\rho}{v_{xy}} = \frac{2\pi}{cB}\frac{m}{Z}. \tag{2.2}$$

In the non-relativistic kinematics regime, the cyclotron period is independent of the particle energy or direction and it only depends on the mass-to-charge ratio and the magnetic field. After completing one cycle, the particle returns to the axis parallel to the magnetic field at a distance

$$z = v_z T_{\mathrm{cyc}} \tag{2.3}$$

from the place where it was emitted from. Measuring the time-of-flight of one cycle provides the mass-to-charge ratio, denoted as A/q, allowing for particle identification.

2.2 Kinematics of two-body scattering

Let us consider the following scenario: a projectile **a** of mass m_{a} with kinetic energy T collides with a target **b** of mass m_{b}. After scattering, the ejectile **1** and recoil **2** of masses m_1 and m_2, respectively, emerge, as shown in Fig. 2.3.

The objective of measurements conducted with solenoidal specrometers is to determine the excitation energy of a compound nucleus (E_x) and the emission

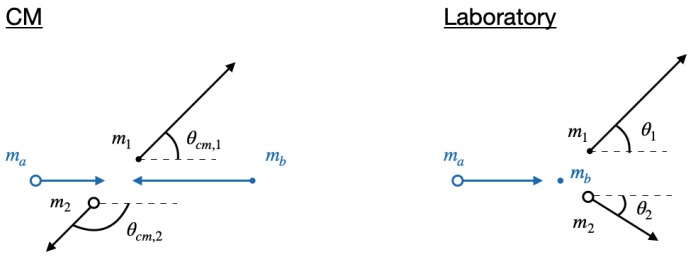

Figure 2.3: Two-body scattering in the center of mass (CM) frame (on the left) and in the laboratory frame (on the right).

angle of the ejectile in the center-of-mass system (θ_{cm}). However, these cannot be directly measured. Instead, what is measured is the laboratory energy (E) of the ejectile proton and the distance of its helical orbit return to the z-axis (z). The masses (m_a, m_b, m_1, and m_2) and the beam velocity are also known. By manipulating the 4-momentum vectors of the reaction products 1 and 2 and applying relativistic mechanics, it is possible to derive expressions for E_x and θ_{cm}, as presented below.

The four-momenta of particles 1 and 2 in the laboratory frame are given by (derivation in Appendix A)

$$\begin{aligned}
\mathbb{P}_1 &= \begin{pmatrix} E \\ p_z \\ p_{xy} \end{pmatrix} = \begin{pmatrix} \gamma q + \gamma\beta p\cos\theta_{\mathrm{cm},1} \\ \gamma\beta q + \gamma p\cos\theta_{\mathrm{cm},1} \\ p\sin\theta_{\mathrm{cm},1} \end{pmatrix} = \begin{pmatrix} E \\ k\cos\theta_1 \\ k\sin\theta_1 \end{pmatrix}, \\
\mathbb{P}_2 &= \begin{pmatrix} E' \\ p'_z \\ p'_{xy} \end{pmatrix} = \begin{pmatrix} \gamma Q + \gamma\beta p\cos\theta_{\mathrm{cm},1} \\ \gamma\beta Q + \gamma p\cos\theta_{\mathrm{cm},1} \\ p\sin\theta_{\mathrm{cm},1} \end{pmatrix} = \begin{pmatrix} E' \\ k'\cos\theta_2 \\ k'\sin\theta_2 \end{pmatrix},
\end{aligned} \tag{2.4}$$

where E and E' are total energies of 1 and 2 in the laboratory frame, θ_{cm} is the center of mass scattering angle, k and k' are the momenta of reaction products 1 and 2 in the laboratory frame, θ is the scattering angle in the laboratory frame. Note that ejectile 1, is the lighter of the reaction products. In the following derivations it is assumed that the speed of light $c = 1$. The magnitude of the velocity divided by the speed of light, β, of the center of mass as seen in the lab frame, and the Lorentz factor, γ, are given by

$$\beta = \frac{k_a}{E_c} = \frac{\sqrt{(T+m_a)^2 - m_a^2}}{m_a + m_b + T}, \qquad \gamma = \frac{1}{\sqrt{1-\beta^2}}. \tag{2.5}$$

where k_a is the initial 4-momentum of a in the laboratory frame, E_c is the total energy of the system, while T represents the kinetic energy of projectile a. Defining E_a as the total energy of a, we get the following dependencies:

$$E_a = T + m_a \Rightarrow T = E_a - m_a = \sqrt{m_a^2 + k_a^2} - m_a. \tag{2.6}$$

By introducing q and Q as the total energy of 1 and 2 in the CM frame, respectively, the total energy E_t in the CM frame or the mass of the system M_c (in the CM frame $E_t = M_c$), and the momentum p of the reaction products 1 or 2 in the center-of-mass frame (CM), one obtains

$$q = \sqrt{m_1^2 + p^2} = \frac{1}{2E_t}(E_t^2 - m_2^2 + m_1^2), \tag{2.7a}$$

$$Q = \sqrt{m_2^2 + p^2} = \frac{1}{2E_t}(E_t^2 + m_2^2 - m_1^2), \tag{2.7b}$$

$$\begin{aligned} M_c^2 = E_t^2 = E_c^2 - k_a^2 = (m_a + m_b + T)^2 - (T + m_a)^2 + m_a^2 = \\ (m_a + m_b)^2 + 2m_b T, \end{aligned} \tag{2.7c}$$

We want to express p in terms of m_1, m_2, and E_t. Using expressions for q and Q, we can write

$$m_1^2 + m_2^2 + 2p^2 = q^2 + Q^2. \tag{2.8}$$

After using Eq. (2.7) for solving the above equation, we get

$$p^2 = \frac{1}{4E_t^2}\left(\left(E_t^2 - (m_2 + m_1)^2\right)\left(E_t^2 - (m_2 - m_1)^2\right)\right). \tag{2.9}$$

Let us now calculate k. We will be using the trigonometric identity:

$$\sin^2\theta_{\mathrm{cm},1} + \cos^2\theta_{\mathrm{cm},1} = 1. \tag{2.10}$$

From Eq. (2.4) we know that:

$$\begin{aligned} -p\sin\theta_{\mathrm{cm},1} = k\sin\theta_1 \quad &\Rightarrow \quad \sin\theta_{\mathrm{cm},1} = \frac{k\sin\theta_1}{p}, \\ \gamma\beta q + \gamma p\cos\theta_{\mathrm{cm},1} = k\cos\theta_1 \quad &\Rightarrow \quad \cos\theta_{\mathrm{cm},1} = \frac{k\cos\theta_1}{\gamma p} - \frac{\beta q}{p}. \end{aligned} \tag{2.11}$$

After solving this in terms of k, two possible solutions are obtained:

$$k = \frac{\frac{\gamma}{\cos\theta_1}}{1 + \gamma^2\tan^2\theta_1}\left(\beta q \pm \sqrt{p^2 + (p^2 - q^2\beta^2)\gamma^2\tan^2\theta_1}\right). \tag{2.12}$$

However, only one of the solutions (the $'+'$ one) has a physical meaning (the other gives negative k).

The basic formula for the curvature radius due to the presence of a magnetic field (Eq. 2.1) is

$$\rho = \frac{p_{xy}}{cZB}. \tag{2.13}$$

Together with the kinematics of the transfer reaction

$$\rho = \frac{p_{xy}}{cZB} = \frac{p \sin\theta_{\mathrm{cm},1}}{cZB}. \tag{2.14}$$

The time for one helix cycle in the magnetic field is given by Eq. (2.2)

$$T_{cyc} = \frac{2\pi\rho}{v_{xy}} = \frac{2\pi}{cZB}\frac{p\sin\theta_{\mathrm{cm},1}}{v_{xy}}. \tag{2.15}$$

The distance covered along the beam axis over one cycle is

$$\begin{aligned} z_0 = v_z T_{cyc} = 2\pi\rho\frac{v_z}{v_{xy}} = \frac{2\pi}{cZB}\frac{v_z}{v_{xy}}p\sin\theta_{\mathrm{cm},1}, \qquad \frac{v_z}{v_{xy}} = \frac{1}{\tan\theta_1}, \\ z_0 = 2\pi\frac{\rho}{\tan\theta_1} = \frac{2\pi}{\tan\theta_1}\frac{p_{xy}}{cZB} = \frac{2\pi}{cZB}\frac{p_z}{p_{xy}}p_{xy} = \frac{p_z}{\alpha}, \qquad \alpha = \frac{cZB}{2\pi}, \end{aligned} \tag{2.16}$$

$$\alpha z = p_z = \gamma\beta q + \gamma p\cos\theta_{\mathrm{cm},1}. \tag{2.17}$$

Together with the energy equation Eq. (2.4), we have 2 coupled equations

$$\begin{cases} \alpha z = \gamma\beta q + \gamma p\cos\theta_{\mathrm{cm},1}, \\ T_1 + m_1 = \gamma q + \gamma\beta p\cos\theta_{\mathrm{cm},1}, \end{cases} \tag{2.18}$$

where T_1 is the kinetic energy of the lighter particle 1 and $T_1 + m_1 = E$.

Particle 2 can become excited. For a small excitation energy $E_x \ll m_2$

$$m_2 \to m_2 + E_x \tag{2.19}$$

2.2.1 The constant E_x line

Let us eliminate $\cos\theta_{\mathrm{cm}}$ in Eq. (2.18). We subtract the first equation from the second one, and after some rearrangements we obtain

$$\begin{aligned} T_1 + m_1 &= \gamma q - \gamma\beta^2 q + \alpha\beta z = \\ &= \gamma q(1-\beta^2) + \alpha\beta z = \frac{1}{\gamma}q + \alpha\beta z. \end{aligned} \tag{2.20}$$

Using Eq. (2.7a) the above expression can be written as

$$\begin{aligned} T_1 &= \frac{1}{\gamma} q - m_1 + \alpha\beta z = \\ &= \frac{1}{2\gamma E_t} \left(E_t^2 + m_1^2 - m_2^2 \right) - m_1 + \alpha\beta z. \end{aligned} \tag{2.21}$$

When the excitation energy E_x is small ($E_x \ll m_2$), Eq. (2.19) can be used

$$\frac{m_2^2}{2\gamma E_t} \to \frac{(m_2 + E_x)^2}{2\gamma E_t} \approx \frac{m_2^2}{2\gamma E_t} \left(1 + \frac{2E_x}{m_2} \right) = \frac{m_2^2}{2\gamma E_t} + \frac{m_2}{\gamma E_t} E_x, \tag{2.22}$$

which yields

$$T_1 = \frac{E_t^2 + m_1^2 - m_2^2}{2\gamma E_t} - \frac{m_2}{\gamma E_t} E_x - m_1 + \alpha\beta z. \tag{2.23}$$

Using Eq. (2.23), the kinetic energy of the proton can be expressed as a function of the distance z and the excitation energy E_x. The dependence is linear, and a $T_1 - z$ plot calculated for several constant excitation energies E_x is shown in Fig. 2.4. An infinitely small detector is considered in Fig. 2.4a. An analogous plot for a finite size detector is shown in Fig. 2.4b (a derivation of equations for a finite-sized detector can be found in Appendix B). The considered detector is a cylindrical tube with a radius of 25 mm. The proton hits the detector before completing a full orbit which causes the knee-like shape for each E_x.

In a (d,p) reaction, states of particle 2 of various excitation energy can be populated. As shown in Eq. (2.23), the different states can be distinguished as separate lines. However, when the state density is very high, which is the case for heavy nuclei, the lines become so densely packed that they can no longer be distinguished.

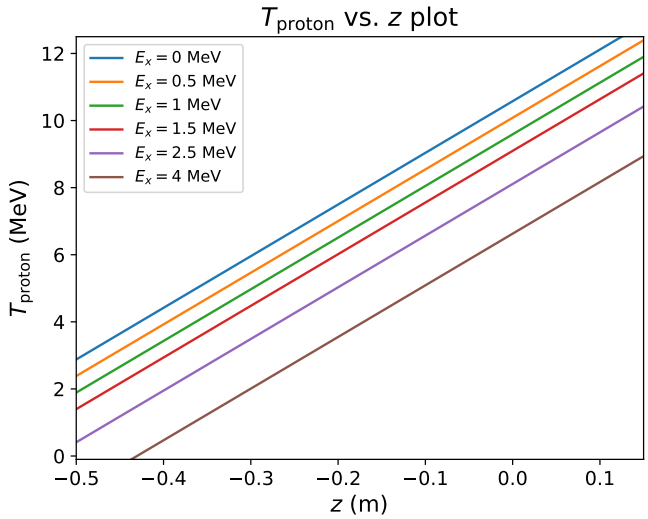

(a)

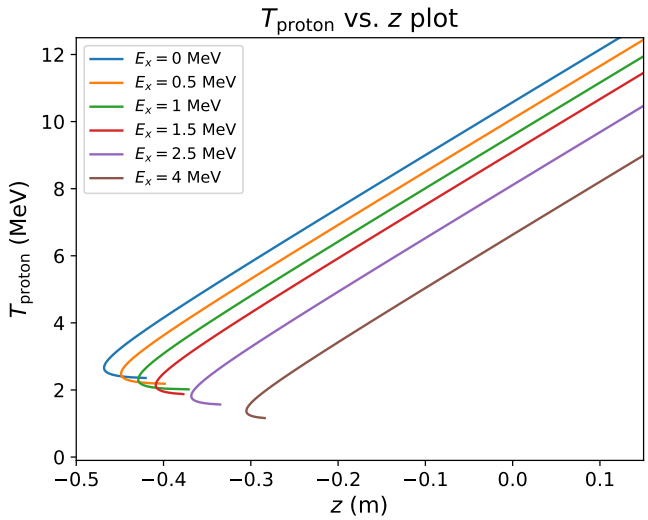

(b)

Figure 2.4: Kinetic energy of the proton as a function of z distance from the target for several excitation energies. The calculated reaction is ^{229}Ac(d,p)^{229}Ac, at a beam energy of 8 MeV/u in magnetic field of 2.5 T (a) for an infinitely small detector, (b) for a detector with a radius of 25 mm.

2.3 The inverse problem

As discussed in the beginning of this chapter, solenoidal spectrometers offer details about the z-coordinate and the energy E deposited by the detected particle (protons for (d,p) reactions). Consequently, the primary objective of the analysis is to convert this information into the excitation energy E_x of the compound nucleus and the emission angle θ_{cm} of the produced proton. We need to find the following transformation

$$\begin{pmatrix} E \\ z \end{pmatrix} \longrightarrow \begin{pmatrix} E_x \\ \theta_{\mathrm{cm},1} \end{pmatrix}. \tag{2.24}$$

By taking Eq. (2.18) and substituting the expressions for q and p derived in Eq. (2.7) using $m_2 \to m_2 + E_x$, one obtains

$$\begin{aligned} E = \frac{\gamma}{2E_t}\Bigg(& M_c^2 + m_1^2 - (m_2 + E_x)^2 \\ & - \beta\cos\theta_{cm,1}\sqrt{\left(M_c^2 - (m_1 + m_2 + E_x)^2\right)\left(M_c^2 - (m_1 - m_2 - E_x)^2\right)}\Bigg) \end{aligned} \tag{2.25}$$

and

$$\begin{aligned} z = \frac{\gamma}{2E_t}\frac{1}{\alpha}\Bigg(& \beta(M_c^2 + m_1^2 - (m_2 + E_x)^2) \\ & - \cos\theta_{cm,1}\sqrt{\left(M_c^2 - (m_1 + m_2 + E_x)^2\right)\left(M_c^2 - (m_1 - m_2 - E_x)^2\right)}\Bigg). \end{aligned} \tag{2.26}$$

The inverse transformation can be calculated by incorporating the expression for $\cos\theta_{\mathrm{cm}}$ derived from Eq. (2.26) into Eq. (2.25), resulting in

$$E_x^2 + 2m_2E_x + m_2^2 - m_1^2 - M_c^2 + 2\gamma E_t(E - \alpha\beta z) = 0. \tag{2.27}$$

After solving this equation in terms of E_x we obtain

$$\boxed{E_x = -m_2 + \sqrt{M_c^2 + m_1^2 - 2\gamma M_c(E - \alpha\beta z)}.} \tag{2.28}$$

By reordering Eq. (2.25), it can be expressed as

$$\begin{aligned} M_c^2 + m_1^2 - (m_1 + E_x)^2 = \frac{2E_t}{\gamma}E + \\ \beta\cos\theta_{cm,1}\sqrt{(M_c^2 - (m_1 + m_2 + E_x)^2)(M_c^2 - (m_1 - m_2 - E_x)^2)}. \end{aligned} \tag{2.29}$$

Combining the above equation and Eq. (2.26) yields

$$\boxed{\cos\theta_{cm,1} = \frac{\gamma(E\beta - \alpha z)}{\sqrt{\gamma^2(E - \alpha\beta z)^2 - m_1^2}}.} \tag{2.30}$$

Using Eq. (2.28) and Eq. (2.30), it is possible to extract the excitation energy of the compound nucleus as well as the proton emission angle based on information on the energy and hit position of the detected proton.

The above derivation considered an infinitely small detector (in $x - y$ direction) placed along the z-axis. In the laboratory, the detector has a radius which cannot be ignored. For a finite-size detector with radius a, the hit position z_{hit} is given by

$$z_{\text{hit}} \approx z\Big(1 - \frac{1}{2\pi}\frac{a}{\rho}\Big), \tag{2.31}$$

and to obtain E_x and $\cos\theta_{\text{cm}}$, numerical methods are required. The derivation of those can be found in Appendix B.

Figs. 2.5 to 2.7 show correlations between E_x, T_1, z, and $\cos(\theta_{\text{cm}})$.

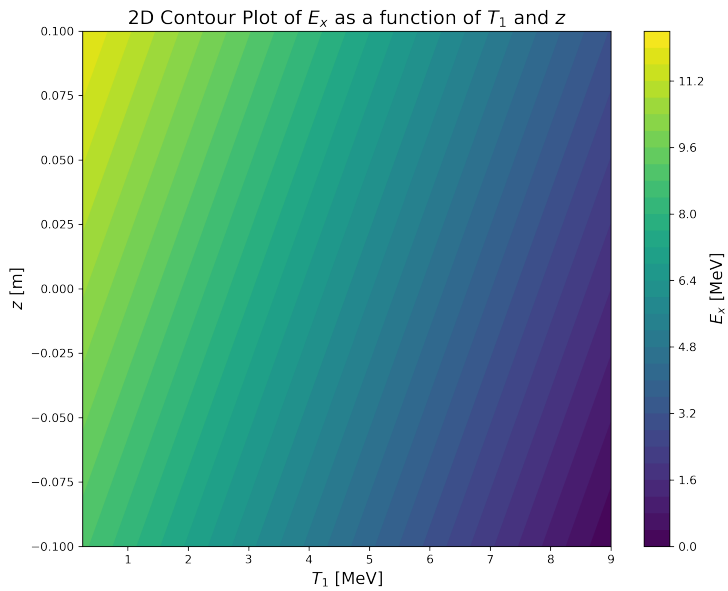

Figure 2.5: Excitation energy of a nucleus (E_x) as a function of the return distance to the axis (z) of the light ejectile and kinetic energy of the light ejectile (T_1). Figure from Ref. [16].

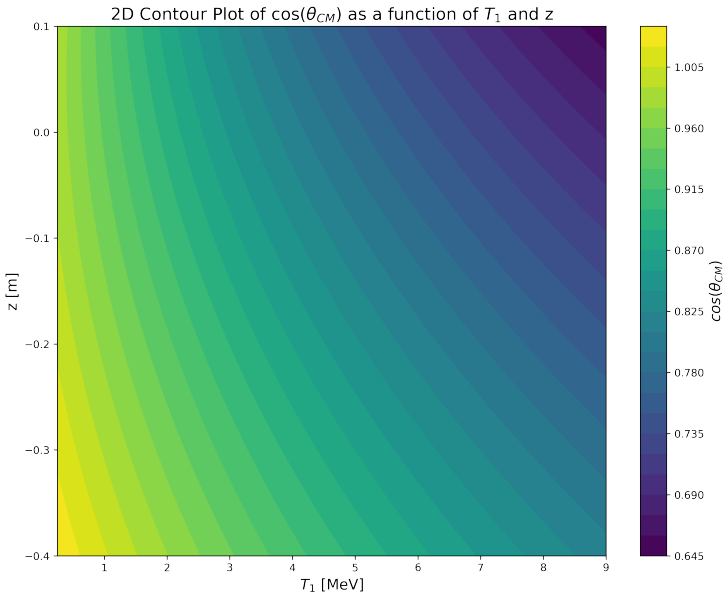

Figure 2.6: Cosine of emission angle of the light ejectile in the CM frame ($\cos(\theta_{\mathrm{cm}})$) as a function of the return distance to the axis (z) and kinetic energy of the light ejectile (T_1). Figure from Ref. [16].

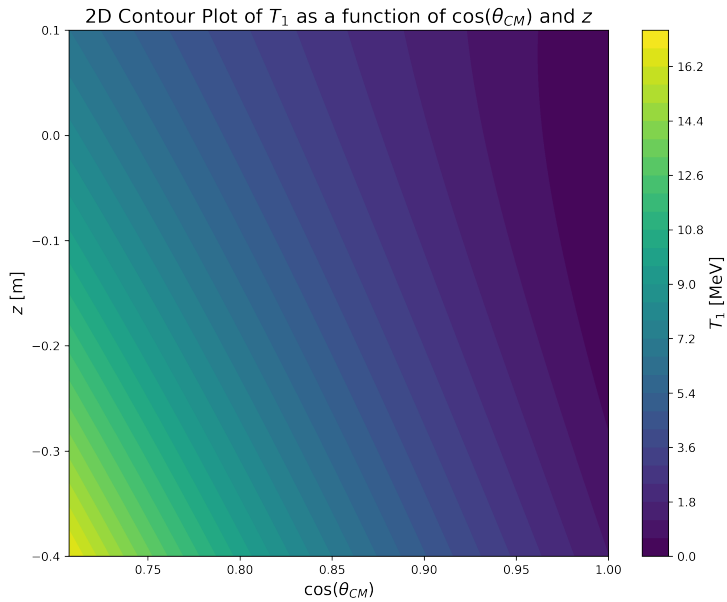

Figure 2.7: Kinetic energy of the light ejectile (T_1) as a function of its return distance to the axis (z) and cosine of its emission angle in the CM frame ($\cos(\theta_{\mathrm{cm}})$). Figure from Ref. [16].

Chapter 3

Proof-of-principle ^{238}U(d,pf) experiment at HELIOS

To investigate if it is possible to study (d,pf) reactions in inverse kinematics in solenoidal spectrometers, a proof-of-principle experiment has been conducted. Fission of ^{239}U was examined using a stable beam of ^{238}U at HELIOS at Argonne National Laboratory (ANL). Fission of ^{239}U has already been investigated by other methods, and fission data are available, including cross sections [17–19], fission barrier heights [20], and fission fragment yield distributions [21, 22]. Therefore, studying the fission of this nucleus and comparing the result with existing data in literature allow to verify whether the transfer-induced fission method is applicable to reliably measure fission barrier heights in other unstable systems, that cannot be investigated through experiments in normal kinematics or by using multinucleon transfer reactions with a stable beam in inverse kinematics.

3.1 Experimental setup

The experiment was conducted using the HELIOS solenoidal spectrometer at ANL [23]. HELIOS consists of a 0.9 m diameter bore and 2.0 m long superconducting solenoidal magnet. The geometry and calculated trajectories of the reaction products are illustrated in Fig. 3.1. The stable ^{238}U beam travels through a hollow four-sided silicon array up to a deuterated polyethylene (CD_2) target. The Si array measures the laboratory energy and hit position of light ejectiles (protons) along the detector after returning to the z-axis.

Downstream from the target, a Faraday cup and an annular silicon detector were installed (not shown in Fig. 3.1). The Faraday cup measured the beam current (needed for beam tuning), and the silicon detector was to used to detect elastically scattered deuterons from the target, enabling to measure absolute fis-

sion probabilities. For fission fragment detection, four gas-filled detectors were used. Each of them consisted of a position-sensitive multiwire proportional counter (MWPC) followed by a Bragg chamber. The Bragg chambers provided information about the energy loss of a given fission fragment in different parts of the chamber, thereby measuring the Bragg peak. This would allow to extract the charge of the fission fragment. The MWPCs provided the position information along with a fast timing signal used to build coincidences between fission fragment detection and hits in the Si array. Two of the fission fragment detectors were positioned at 15° with respect to the beam axis, and two at 10° to maximize the acceptance of light and heavy fission fragments, respectively [24]. The 15° and 10° detectors were mounted in pairs at opposite azimuthal angles, such that one of each kind would be hit for the same event.

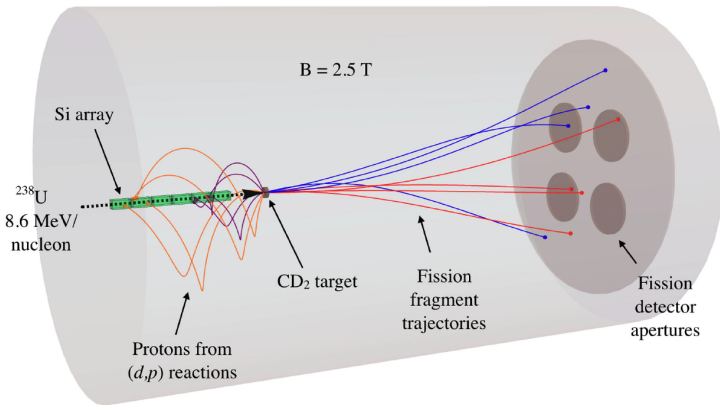

Figure 3.1: Schematic picture of the experimental setup for the ^{238}U(d,pf) experiment. The silicon array for proton detection is placed upstream from the CD_2 target. The fission fragment detectors are placed downstream at the rear of the magnet. Example helical trajectories of protons and fission fragments are shown. The orange trajectories correspond to trajectories with different center of mass (CM) angles for reactions populating the ground state in ^{239}U, and the purple curves correspond to states at 7 MeV excitation energy. The blue trajectories correspond to fragments with $A = 100$, whereas the red ones correspond to $A = 138$. Figure from Ref. [24].

For the experiment, 11 CD_2 targets with a thickness of 410 – 590 μg/cm^2 were used. The change of targets during the experiment was necessary because of target damage by the heavy uranium beam. To measure the background originating from multinucleon transfer-induced fission reactions on carbon within the CD_2 target, measurements with a target made of natural carbon were also performed.

The beam of ^{238}U at an energy of 8.6 MeV/u was provided by the ATLAS accelerator. The average beam intensity reached approximately 10^6 particles per second (pps), resulting in a total integrated beam dose of approximately 5.5×10^{11} ions.

3.2 Calibration and data analysis

The experimental data have been analysed and published [24], demonstrating consistency with existing ^{239}U fission data. Additionally, the recorded raw data has been shared with the author of this licentiate thesis for a crosscheck and to gain experience in this type of calibration and data analysis. Details of the calibration and data analysis conducted by the author of this thesis are presented in the following sections. The routines developed here will be used during on- and offline analysis of future experiments.

3.2.1 Calibration of the silicon array

To detect the ejectile protons, the HELIOS silicon-detector array was used. It consists of 24 position-sensitive silicon detectors (PSDs) mounted on a four-sided aluminium rod, six detectors on each side, see Fig. 3.2.

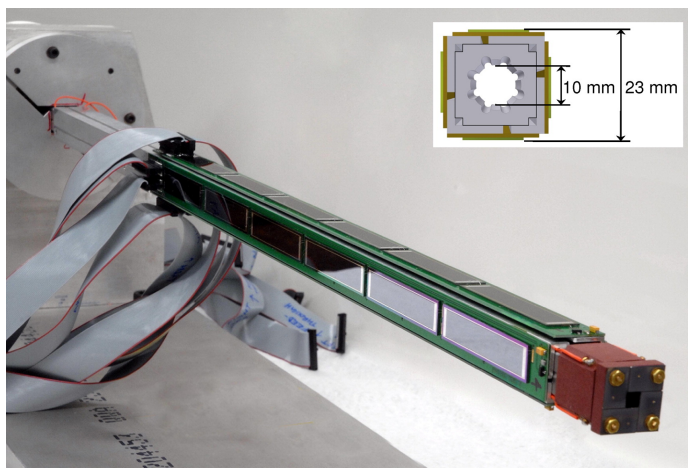

Figure 3.2: The HELIOS silicon-detector array. Six detectors are mounted on each of the four sides. The target would be in the lower-right corner of the picture. For the ^{238}U(d,pf) experiment, the distance between the array and the target was 55 mm. The red piece in front shields the array from low energy protons which complete multiple turns in the magnetic field before hitting the array (multi-turn protons). Figure from Ref. [13].

A photograph of one of the PSDs from the Si array is shown in Fig. 3.3. The silicon wafer is mounted on a printed circuit board. Each PSD has 3 readout channels: the total energy output c_t at the back face, and two energy readouts at both edges of the front face of a detector, c_n and c_f. There is a resistance of approximately 17 kΩ between the front edges of a detector, and using resistive division between c_n and c_f, the position of the hit along the z-axis can be extracted.

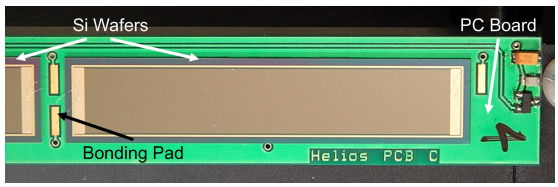

Figure 3.3: One Si PSD from the HELIOS Si array. There are electrical contacts at both short edges of the front face of each PSD (the lighter-colour part of a PSD) as well as one full-area contact at the back face. Figure from Ref. [13].

After calibration, the total energy is given by:

$$E_t = k_t \cdot c_t + m_t, \tag{3.1}$$

where k_t and m_t are calibration parameters.

For the energy calibration of the c_t readout channels, i.e. to determine the slopes, k_t and offsets, m_t, for all detectors, α radiation from a ^{228}Th source was used. The analysis considered the seven strongest peaks, as presented in Table 3.1:

Parent nucleus	Parent E (MeV)	Parent J^π	Parent $T_{1/2}$	Energy of alpha (MeV)
^{228}Th	0	0^+	1.9125 y	5.340
^{228}Th	0	0^+	1.9125 y	5.423
^{224}Ra	0	0^+	3.66 d	5.685
^{212}Bi	0	1^-	60.55 m	6.050
^{220}Rn	0	0^+	55.6 s	6.288
^{216}Po	0	0^+	144.0 ms	6.778
^{212}Pb	0	0^+	0.299 μs	8.785

Table 3.1: Alpha energies in MeV for a ^{228}Th source. Data from [25–29].

The fitting procedure operates automatically within a fitting script and works in the following way: initially, a maximum of 7 peaks in the spectrum are

identified. The initial parameters for each peak are estimated (mean location, width (σ), and amplitude) and passed to a `nGauss` (3.2) function, which is then fitted to the entire spectrum. Subsequently, the parameters of each peak are extracted and stored. Each step is illustrated in Fig. 3.4.

The tabulated energy values (see Table 3.1) and the fitted peak positions in channels are now known. However, there is a possibility that the peak finder may have identified a false peak or missed one of the wanted peaks, potentially causing problems when matching the fitted peaks to the tabulated energy values. To handle this, all sorted 4-element combinations of the fitted peaks (x) are generated. At the same time, 4-element combinations of the tabulated energy values (y) are also created, where the 4-element combinations are all possible arrangements of any four tabulated energy values out of seven. Subsequently for all (x, y) pairs, each x_i is matched with its corresponding y_i, where the index i refers to the index in the 4-element, and a linear fit is performed for these (x_i, y_i) pairs of 4-element combinations. From all these linear fits, the one with the lowest χ^2 is selected (i.e., the most linear case). This fit provides us with pre-fit parameters, namely k'_t and m'_t. With these parameters, we can then reconstruct an `nGauss` function,

$$\texttt{nGauss} = \sum_{i=1}^{7} A_\mathrm{i} \exp\left(-\frac{1}{2\,\sigma^2}\left(x - \frac{r_\mathrm{i} - m_\mathrm{t}}{k_\mathrm{t}}\right)^2\right), \tag{3.2}$$

where A_i is the amplitude of each peak, σ is the standard deviation (uniform across all peaks), r_i is the tabulated energy value, and k_t and m_t are the parameters of interest. By fitting Eq. (3.2) to the raw energy spectrum, k_t and m_t are obtained. The calibrated energy spectrum for one of detectors is shown in Fig. 3.5.

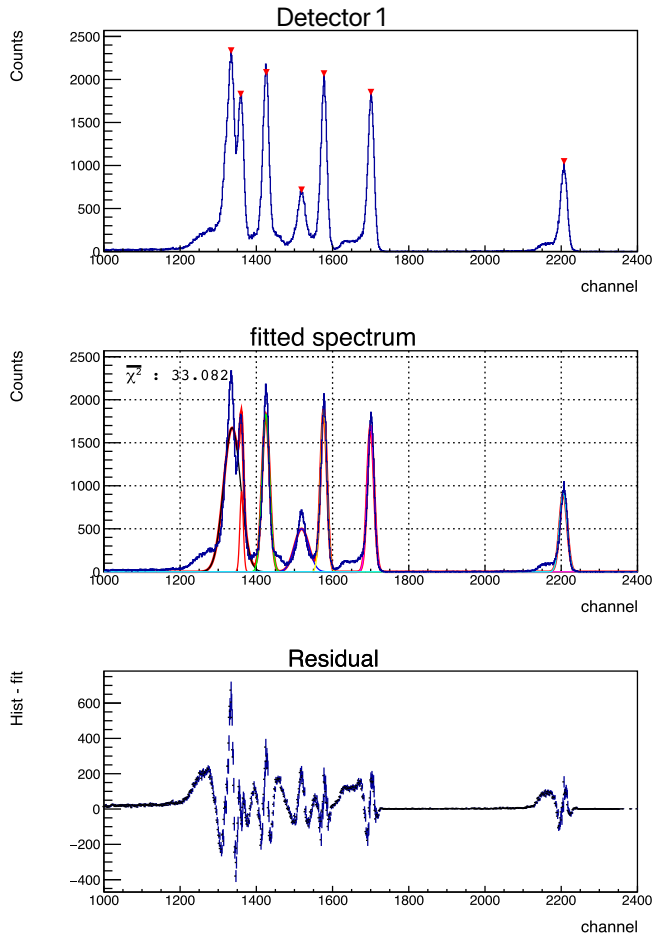

	count,	mean,	sigma
1,	67029(326),	1336.5507(0.1091),	22.3726(0.1112)
2,	7523(192),	1361.3273(0.1084),	4.4848(0.0837)
3,	33061(196),	1424.9675(0.0705),	10.1039(0.0676)
4,	16757(136),	1518.8949(0.1601),	18.7247(0.2893)
5,	28458(200),	1576.8142(0.0646),	8.4503(0.0534)
6,	27261(182),	1699.8356(0.0752),	8.9817(0.0616)
7,	16321(161),	2205.5520(0.0892),	10.0143(0.0757)

Figure 3.4: The first step of fitting of the c_t spectrum is illustrated in the following manner: the top plot shows peaks identified using the `Search` method from the ROOT [30] `TSpectrum` class; the middle plot displays the fitted spectrum (at most maximum 7 separately fitted peaks as well as their sum); the lowest plot exhibits the original c_t spectrum with the subtracted fitted function. Parameters for each individual peak, along with their corresponding errors, are provided below the plots.

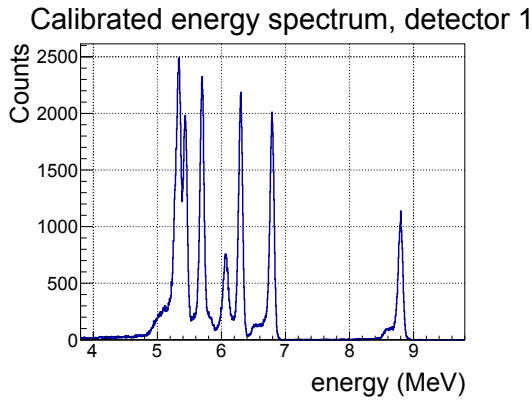

Figure 3.5: Calibrated energy spectrum from detector 1.

Raw c_f and c_n signals of detector 19 are shown in Fig. 3.6. For fixed deposited energies, there are linear relations between c_f and c_n, and the lines of different α-decays can be distinguished. Thus, c_n can be expressed as a function of c_f:

$$c_\mathrm{f} = a \cdot c_\mathrm{n} + b, \tag{3.3}$$

where a and b are constants.

The a and b coefficients can be obtained by plotting c_f vs c_n with a gate on c_t belonging to an energy peak within a 2σ region, and performing a linear fit.

To gain-match the three signals for each detector, a linear relationship of the following form was employed:

$$c_\mathrm{t} = d(c_\mathrm{f} + a\, c_\mathrm{n}) + f. \tag{3.4}$$

For each detector, $c_\mathrm{f} + a\, c_\mathrm{n}$ versus c_t is plotted, as shown in Fig. 3.7. The coefficients d and f from Eq. (3.4) are obtained by performing a linear fit to such plots.

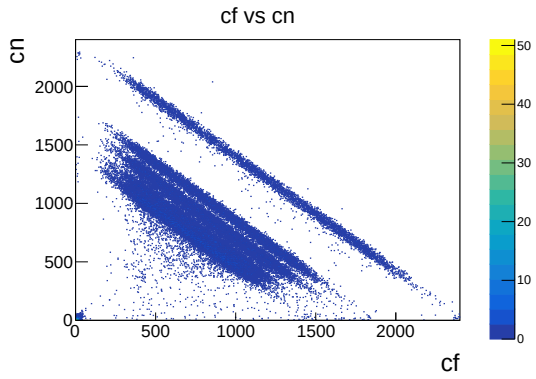

(a)

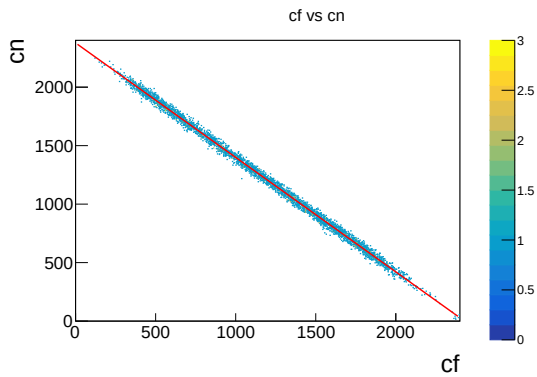

(b)

Figure 3.6: (a): Plot of the opposite side signals of one detector, c_f vs c_n, for a ^{228}Th α source. There is a linear relation between c_f and c_n, such that the α-lines can be distinguished. (b): The same plot gated on c_t belonging to an energy peak within a $\pm 2\sigma$ region as well as a linear fit (indicated as red line).

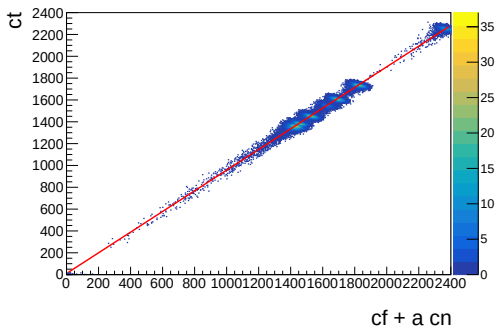

Figure 3.7: Plot of scaled sum of energy outputs at both sides of a detector, $c_\mathrm{f} + a\, c_\mathrm{n}$, vs the total energy output at the back face, c_t. The coefficients d and f of Eq. (3.4) are obtained by performing a linear fit to the above plot (indicated as red line in the plot).

The relative position of a hit along a PSD can be represented as u, $u \in (-1, 1)$: $u = \frac{c'_\mathrm{f} - c'_\mathrm{n}}{c_\mathrm{t}}$, where c'_f and c'_n are gain matched to the energy signal c_t: $c'_\mathrm{f} = d\, c_\mathrm{f} + f$, and $c'_\mathrm{n} = d\, a\, c_\mathrm{n} + f$.

The c_f and c_n signals are induced by resistive division of charge induced in the PSD by a particle depositing its energy. When a particle hits in the centre of a PSD, there is an equal amplitude signal for both c_f and c_n. It could be that a particle hits very close to one side of the detector, for example the f edge, and induces a high-amplitude c_f signal. At the same time, the corresponding c_n would be small and depending on the electronics settings, it could be below the detection threshold. In principle, 3 situations are possible:

1. both c_f and c_n are available,
2. only c_n is available and c_f is missing,
3. only c_f is available and c_n is missing.

Thus u can be calculated in three ways:

1. $$u = \frac{c'_\mathrm{f} - c'_\mathrm{n}}{c_\mathrm{t}}, \tag{3.5}$$
2. $$u = 1 - \frac{2c'_\mathrm{n}}{c_\mathrm{t}}, \tag{3.6}$$

3.

$$u = \frac{2c'_{\mathrm{f}}}{c_{\mathrm{t}}} - 1. \tag{3.7}$$

Fig. 3.8 illustrates the resulting position spectrum for detector 1. As observed, there are peaks at the minimum and maximum ends of the spectrum. These peaks arise from the electrical contacts located at the edges of each detector, as can be seen in Fig. 3.3. When a particle deposits energy below the contact, the induced signal has maximum amplitude since there is no resistive sharing with the far end contact, and the precise hit position cannot be determined more precisely than that the hit is in the contact region. To address this, a procedure that involves scaling the u values, enforcing them to be within the range of -1 and 1 was used.

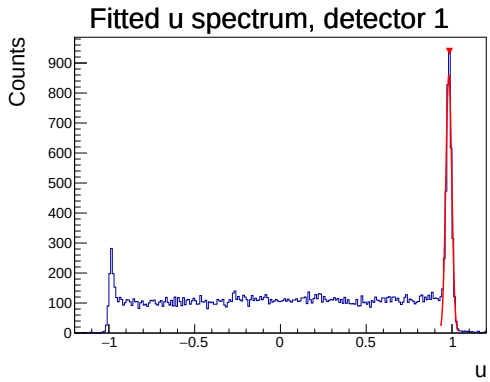

Figure 3.8: Calculated position spectrum for detector 1 in dimensionless units $[-1, 1]$. The peaks on the edges correspond to the regions of electrical contacts at the edges of the detector. The red line indicates a Gaussian fit to one of the peaks.

Finally, the absolute hit position along the z-axis can be calculated as:

$$z = (u - 1)\frac{l}{2} - d_{\mathrm{target}} - d_{\mathrm{i}}, \tag{3.8}$$

where l is the length of one PSD, d_{target} is the distance between the upstream edge of the active area of the Si array and the target, and d_{i} is the distance from the end of the Si array to the centre of detector i.

3.2.2 Results

Once the signals from the Si array are calibrated, the excitation energy for each event with a hit in the Si array can be calculated using the equations described

in Chapter 2 (Eq. (2.28)) and Appendix B. Our focus lies on fission events, where a proton is detected in coincidence with fission fragments. As outlined in Ref. [24], the geometric efficiency of the fission fragment detectors was about 10% for the detection of one of two fission fragments and only 1% for the simultaneous detection of both fission fragments. Since requiring simultaneous detection of two fission fragments reduces the statistics by a factor of 10, it is for this analysis assumed that a fission event is characterized by a hit in the Si array and one or two hits in the fission fragment detectors.

Fig. 3.9 illustrates the time between a hit in the Si array and a hit in a MWPC. For establishing coincidences, a cathode signal from a MWPC was used due to its faster signal response with respect to the Bragg chamber. A distinct peak is observed between -200 ns and 50 ns. Accordingly, a time gate for coincident events is set within that 250 ns time window. The background of time-random coincidences remains relatively constant, except for a minor peak around 200 ns.

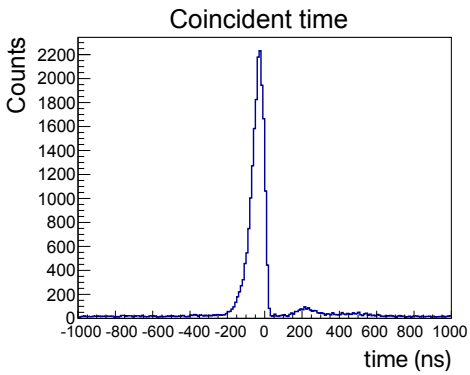

Figure 3.9: Coincident time between a hit in the Si array and a hit in a MWPC. A distinct peak is visible between -200 ns and 50 ns. The background of time-random coincidences remains relatively constant, except for a minor peak around 200 ns.

As discussed in Section 3.1, the excitation energy spectra obtained from measurements exhibit a notable background, potentially arising from multinucleon transfer-induced fission reactions on carbon within the CD_2 target. To determine this background, measurements with a target made of $^{\text{nat.}}$C were conducted. The resulting excitation energy spectra for data acquired with both the CD_2 and the $^{\text{nat.}}$C targets as well as their difference are shown in Fig. 3.10. The upper panel displays excitation energy spectra obtained for all events with a hit in the Si array (referred to as *singles*), where no coincidence with the detection of a fission fragment is required. The lower panel presents the same

data but additionally gated on the detection of one or two fission fragments in the MWPCs within the 250 ns time-coincidence window (*coincidences*).

The natural carbon target data were scaled to align with the CD_2 target data. The procedure involved selecting a region where the $^{nat.}$C and CD_2 target data exhibit a similar shape ($-3 \leq E_x \leq 0$ for singles and $-3 \leq E_x \leq 2$ for coincidences). The scaling factor was determined to be 1.92 for singles and 1.85 for coincidences.

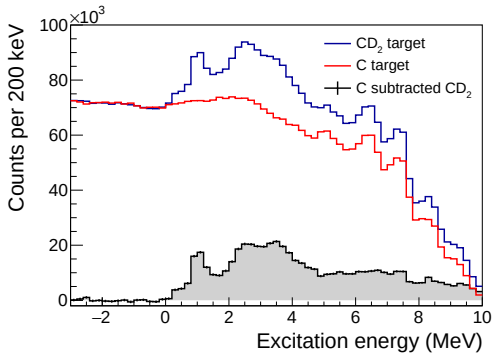

(a)

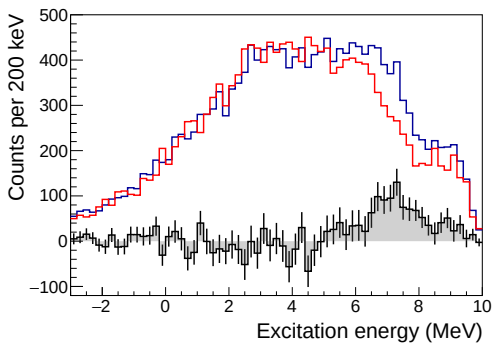

(b)

Figure 3.10: Excitation energy spectra for (a) all events with a hit in the Si array, without a coincidence requirement with a fission fragment. (b) The same data but in addition gated on the detection of one or two fission fragments in the MWPCs. Spectra for data acquired with both the CD_2 and the $^{nat.}$C targets as well as their difference (shaded) are illustrated.

The fission probability as a function of excitation energy E_x of the compound

nucleus can be expressed as:

$$P_f\left(E_x\right) = \frac{N_{d,pf}\left(E_x\right)}{N_{d,p}\left(E_x\right) \cdot \epsilon_f}, \tag{3.9}$$

where $N_{d,p}$ is the number of (d,p) events and $N_{d,pf}$ is the number of (d,pf) events followed by fission, both within a certain excitation energy bin. The ϵ_f is the the total efficiency for detecting a fission event. The calculation of this detection efficiency was not done by the author of this thesis. The detection efficiency for protons cancels out.

The unscaled fission probability as a function of excitation energy is presented in Fig. 3.11. The vertical line presents the known fission-barrier height of ^{239}U (B_f = 6.46 MeV [20]). There is an increase in the unscaled fission probability around E_x = 6.5 MeV, which is consistent with the known fission barrier.

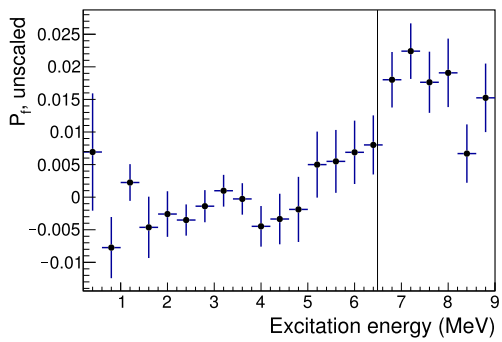

Figure 3.11: The unscaled fission probability of ^{239}U as a function of excitation energy. The vertical line shows the known fission-barrier height value (6.46 MeV [20]).

When comparing the figure above with the fission probabilities depicted in Fig. 3 of Ref. [24], it becomes evident that, although similar in shape, there are some discrepancies between the results. These differences could arise from variations in the calibration procedures used. Additionally, in the analysis conducted for this licentiate thesis, no energy gates were applied to the particles registered in the silicon array. Removing very high-energy particles from the analysis is more likely to suppress background interference. However, such considerations were beyond the scope of the presented simple analysis.

Chapter 4

Experiments with radioactive beams

To study exotic and short-lived isotopes, we have to use radioactive beams. This chapter will cover the production of radioactive elements at the ISOLDE facility at CERN. Following that, the fission experiment of ^{230}Ac, which is planned to be performed using the ISS, will be discussed.

4.1 The ISOLDE Facility at CERN

The ISOLDE Facility is a nuclear physics laboratory at CERN in Geneva, Switzerland. The main focus of ISOLDE is the production of radioactive nuclei with the on-line isotope mass separation technique and experiments with those.

At ISOLDE, more than 1000 isotopes of 74 elements can be produced. As the number of available beams increases, it becomes possible to explore areas of the nuclear chart that have never been studied before, including neutron-rich actinides (see Ref. [31]).

4.1.1 Beam production

Radioactive isotope production at ISOLDE is executed as follows. First, negative hydrogen ions H^- are accelerated in the CERN Linear accelerator 4 (LINAC4) to an energy of 160 MeV. After that, the ions are transferred to the Proton Synchrotron Booster (PSB). During injection into the PSB, two electrons are removed from each H^- ion using a stripping foil, leaving only a proton [32]. In the PSB, the protons are accelerated to an energy of 1.4 GeV. After the acceleration, the now pulsed proton beam with an average current up to 2.0 μA is transferred and impacts directly onto an around 20 cm thick ISOLDE target positioned in a tubular tantalum target container. The path

H^- ions and protons take to reach the destination can be seen in Fig. 4.1, which shows the CERN accelerator complex.

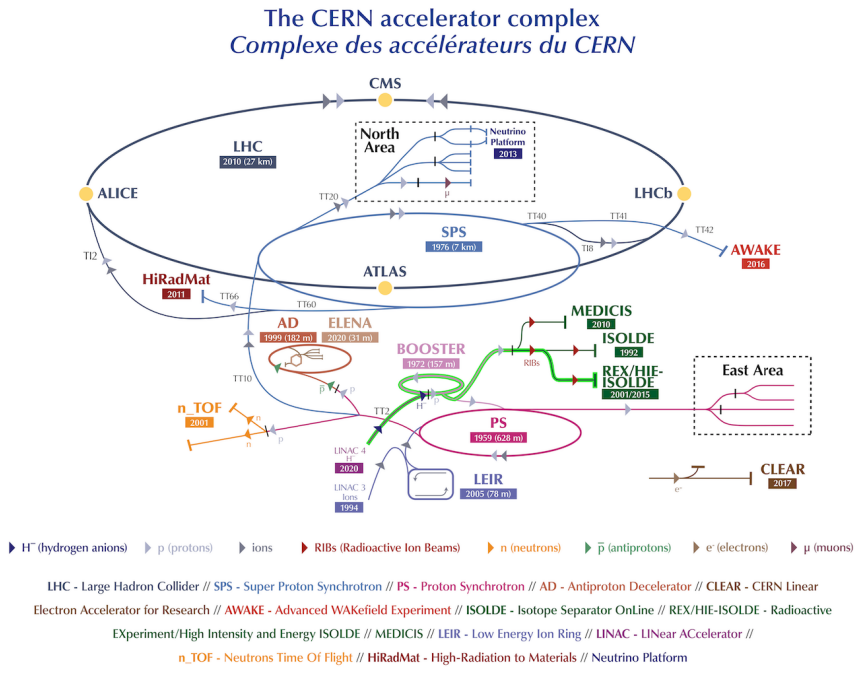

Figure 4.1: The CERN accelerator complex. Negatively-charged hydrogen ions, delivered from LINAC4, are injected into the PSB. During the injection, two electrons are removed from each ion. Then protons are accelerated to an energy of 1.4 GeV. The pulsed proton beam is extracted from the PSB into an ISOLDE target, from where radioactive beams are further distributed to experimental stations. The path H^- ions and protons take to reach ISOLDE is marked in green. Figure adapted from Ref. [33].

As the proton beam impacts the ISOLDE target, fission, spallation, and fragmentation reactions can take place, creating a plethora of different isotopes. Reaction products, trapped in the thick target, can be released by heating the target container (up to 2000°C). The target material needs to be carefully chosen to fit the experimental needs.

The next step is ionization of the extracted isotopes to a 1^+ state. There are three different ion sources that can be used: surface ion sources, plasma ion sources, and laser ion sources. In surface ion sources, ions can be ionized by

passing them through a metal tube (such as tantalum or tungsten) that captures electrons from them. Plasma ion sources operate by ionizing a gas mixture (typically Ar and Xe) through electrons accelerated between the transfer line and the extraction electrode with a voltage of about 130 V, all within a magnetic field. Laser ion sources utilize multi-step photo-ionization.

To then select the isotope of interest, the ionised beam is sent through a mass separator. At ISOLDE, one of two on-line mass separators can be used – the General Purpose Separator (GPS) and the High Resolution Separator (HRS). The GPS's mass resolution $m/\Delta m$ is approximately 800 and allows for simultaneous extraction of two more beams in addition to the central beam. The HRS's mass resolution has been measured to be approximately 6000 [34].

4.1.2 Post-acceleration

Isobars are selected using electric dipole magnets and this mass separated beam is then sent either to the low-energy beam lines or, after charge breeding, to the superconducting post accelerator and the HIE-ISOLDE [4,5] experiments.

The mass-separated beam with energies up to 60 keV/u can be directed into low-energy beam lines. However, in certain fields of research involving radioactive nuclei, the use of beams with energies in the order of MeV/u is crucial. To meet this need, REX- and HIE-ISOLDE post-acceleration installations have been developed. REX-ISOLDE is capable of post-accelerating nuclei to energies of up to 3 MeV/u, while HIE-ISOLDE is anticipated to reach energies as high as 10 MeV/u. This subsection will focus on the design and performance of REX-ISOLDE.

After the ions are mass-separated, the continuous beam (with varying intensity) from a mass separator needs to be cooled, bunched, and charge-bred in order to post-accelerate it.

First, the beam is injected into REXTRAP – a large, gas-filled Penning trap surrounded by a superconducting solenoid. It accumulates the beam, which is first slowed down by the potential of the trap at the entrance to energies of the order of eV. The beam enters a high magnetic field of 3 T and is then further cooled down by collisions with the atoms of a buffer gas. After accumulation the beam is extracted in bunches from the REXTRAP by an electric potential reverse to the one at the entrance, thus the ions retain the original energy they had when they entered. For the process to be effective, the cooling time inside the trap needs to be at least 10 ms [35]. REXTRAP has about 50–60% combined transmission efficiency for the injection, cooling, and extraction processes.

Subsequent to leaving REXTRAP, the beam is directed into EBIS, an Electron Beam Ion Source where 1^+ ions are bred to a higher charge state to make further acceleration more efficient. To be able to trap the 30–60 keV ions coming from REXTRAP, the EBIS is situated on a high-voltage platform. The ions are trapped inside the EBIS by an electrostatic barrier. Low-charged ions,

when trapped, undergo a step-wise ionization through collisions with a dense electron beam from an electron gun. This continues until the ions are eventually extracted. The entire process leads to the distribution of charge states in the outgoing ions. The chosen breeding time depends on the required charge state and may range from milliseconds for light ions up to hundreds of milliseconds for heavy nuclei. The EBIS efficiency varies in between a few percent to forty percent, depending on the beam. More technical details about the EBIS can be found in Ref. [36].

Following their extraction from the EBIS, the ions are directed into a mass-separator to choose a specific charge state and suppress the residual gas. The mass-separator system consists of an electrostatic 90° cylinder deflector and a 90° magnetic bender. Then the ions are injected into the linear accelerator of REX-ISOLDE. The first element of the REX-ISOLDE LINAC is the Radio-Frequency Quadrupole (RFQ), which accelerates ions from 5 keV/u to 300 keV/u. The beam is rebunched in order to fit into the following Interdigital-H-type (IH) structure. The IH structure is a drift-tube which further accelerates the beam to an energy of 1.2 MeV/u. Following this, the beam is directed to three 7-gap spiral resonators and a 9-gap resonator. The final energy of the beam may reach maximum 3 MeV/u for beams of $A/q \leq 4.5$. The LINAC achieves a transmission of approximately 90%.

A schematic diagram of the ISOLDE layout with post-acceleration is shown in Fig. 4.2.

4.1.3 HIE-ISOLDE

HIE-ISOLDE is an energy upgrade of ISOLDE which allows to increase the energy of the radioactive ion beams (RIBs) from 3 MeV/u up to 10 MeV/u [38]. It consists mainly of superconducting cryomodules. The energy upgrade installation is structured into three separate phases. During the initial phase, two cryomodules were added to the existing REX-ISOLDE LINAC. That allowed to increase of the energy up to 5.5 MeV/u. In the second phase, an additional pair of cryomodules was included in order to reach an expected beam energy of 10 MeV/u for $A/q = 4$. In the last phase, the 7-gap resonator and 9-gap structure of REX-ISOLDE are planned to be substituted with two cryomodules, enabling an energy range from 0.45 to 10 MeV/u.

4.2 The ISOLDE Solenoidal Spectrometer

The ISOLDE Solenoidal Spectrometer (ISS) is an experimental setup at HIE-ISOLDE. The design of the ISS draws its inspiration from HELIOS at ANL [23]. It consists of a former-MRI magnet operating at a maximum of 2.5 T (the maximum magnet field of 4 T cannot be used due to safety restrictions in

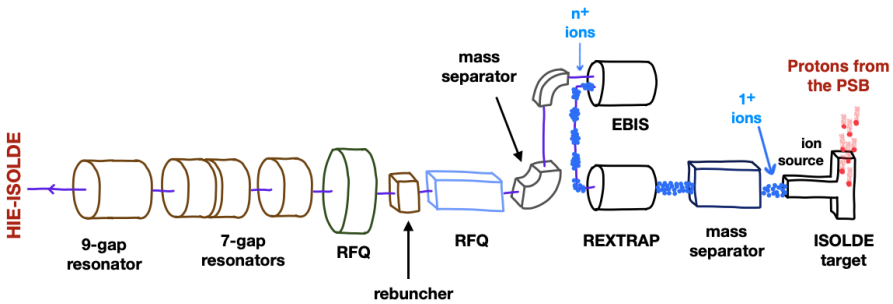

Figure 4.2: Schematic diagram of the ISOLDE–REX-ISOLDE–HIE-ISOLDE layout. Protons from the PSB impinge onto a thick ISOLDE target. Reaction products are released by heating the target and are then ionised to an 1^+ state. The ionised beam is sent trough a mass separator to select the isotope of interest. After being mass-separated, the low-energy beam is post-accelerated with REX-ISOLDE. First, the beam is bunched with REXTRAP. Then it is charge-bred using EBIS which allows to subsequently accelerate it efficiently with a sequence of RFQs and resonators. Figure adapted from Ref. [37].

the ISOLDE hall). The ISS was developed for inelastic scattering and transfer reactions studies mainly using (d,p) reactions, where the detection of the proton allows for good energy resolution. Reactions take place inside the solenoidal field, and reaction products deposit their energy in detectors placed inside the magnet on a dedicated platform.

More details about the detectors planned to be used in the proposed experiment will be provided in the following sections.

4.3 Fission of ^{230}Ac

The path of the r-process lies far away from the $\beta-$stability line and includes highly neutron-rich nuclei. Our interest lies in exploring fission of these isotopes. Given their low stability and the technical challenges in their production, beams of such isotopes are presently unavailable. Our approach involves examining the fission of alternative less-exotic neutron-rich isotopes (which lie closer to the $\beta-$stability line) to establish a measurement method. This methodology aims to be transferable to other, even more neutron-rich nuclei. Furthermore, model predictions for nuclei within our experimental reach can be tested, thereby increasing their predictive power for isotopes we cannot reach, i.e. those relevant for the r-process.

As the initial physics case for an experiment of this kind, the study of fission of ^{230}Ac has been selected. This choice is motivated by several factors: available beam intensities, anticipated fission probabilities, and the absence of definitive fission data at low excitation energies for this particular isotope.

ISOLDE is capable of delivering a 8 MeV/u ^{229}Ac beam with an intensity of 1.3×10^7 pps which would allow for sufficient statistics to successfully run the experiment. In order to achieve such beam rates, the ^{229}Ac needs to be extracted in a molecular form as ^{229}AcFF$^+$ from a ThC_x (thorium carbide) or UC_x (uranium carbide) target with a plasma ion source. Yields above 10^7 μC^{-1} ^{229}AcFF$^+$ have been measured for a UC_x target and a plasma ion source combination at target temperatures above 2000°C. Predictions from FLUKA simulations [39] indicate even higher production rates for ThC_x within the target (1.8×10^{10} μC^{-1} vs. 3.3×10^8 μC^{-1} for UC_x). It is expected that the produced beam will not contain significant contaminants, as proven in the ISOLTRAP MR-ToF MS [40] study of the beam composition of ^{229}AcFF$^+$ [41].

Currently, there are no conclusive data on fission of ^{230}Ac at low excitation energies. It is important to highlight that data exists from two experiments involving ^{230}Ac. The first experiment recorded two inconclusive $\beta-$delayed fission events in mica photo-emulsion foils[1] [42], while the second experiment concentrated on heavy-ion-induced fission at high excitation energies [43], focusing on the extraction of fission transient times (the time fission takes).

There are few predictions of the ^{230}Ac fission barrier height. A fission barrier of 5.37 MeV [44] is extracted in a study conducted by Eckert et al. in 1990 [45], which investigated the fission of highly excited target residue nuclei resulting from collisions between ^{40}Ar and ^{232}Th. A prediction of a 7.01 MeV fission barrier is available from the General Description of Fission Observables (GEF) model [46]. Another estimation places the fission barrier between 5.7 and 6.8 MeV [47], derived from the analysis of the aforementioned two $\beta-$delayed fission candidate events [42]. For experiment planning, the more challenging value of 7.01 MeV is assumed.

In the upcoming experiment, in addition to measuring the fission barrier height, there are plans to conduct measurements of the γ radiation emitted during fission. The information on the total energy of γ rays holds astrophysical significance as it provides information on how much energy in the form of γ-rays is available after fission. This information can be used in r-process models. Simultaneously, analysis of the multiplicity of emitted γ rays aims at a better understanding of angular momentum generation in fission processes [48].

[1] Mica is a material that belongs to a group of silicate materials. It has excellent thermal and electrical insulating properties.

4.3.1 Experimental setup

In order to successfully measure the fission barrier height and the fission cross section of ^{230}Ac, several observables need to be determined. First, the detection of back-scattered protons in coincidence with fission fragments is crucial to establish whether a (d,pf) reaction has occurred. By measuring the energy and hit position of the protons, the excitation energy E_x of the fissioning system can be calculated using Eq. (2.28). Subsequently, the fission barrier height can be determined as a function of E_x. To obtain the fission cross section, it is essential to calculate the product of the beam intensity and the number of target particles per unit area, which can be determined by measuring elastically scattered deuterons within a specified angular range. Lastly, the measurement of γ rays emitted from fission fragments enables extraction of their total energy and multiplicity.

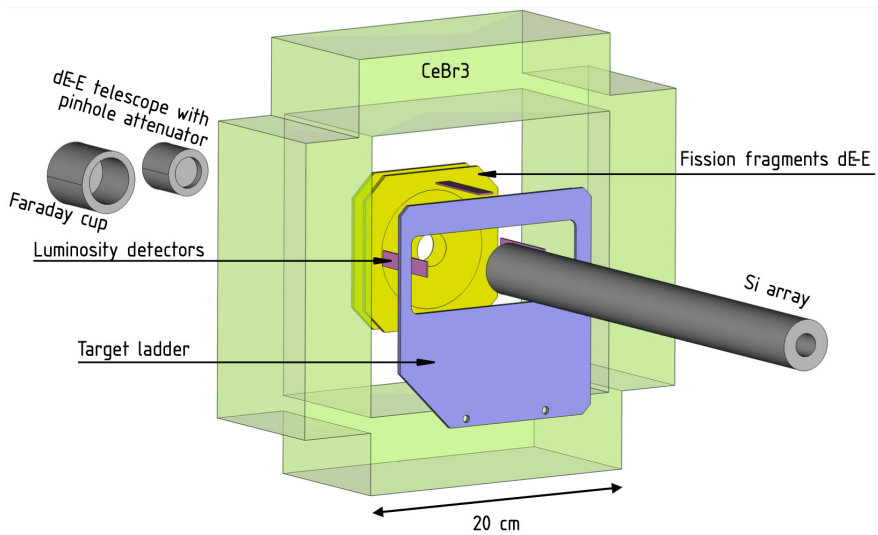

Figure 4.3: Schematic illustration of the detectors inside the vacuum chamber of the ISS magnet. For tuning and beam monitoring, the Faraday cup and the ΔE-E telescope with the pinhole attenuator are mounted on a movable support. Only one of those parts of the setup will be used at any given time. Beam enters from the lower right through the hollow upstream silicon array and impinges on the target. Deuterons elastically scattered from the target are detected by the four luminosity detectors. Fission fragments move in the forward direction and are detected by the ΔE-E CD-shaped Si detector. Gamma-rays emitted from the fission fragments are detected by a $CeBr_3$ detector array. Except for beam monitor detectors, all dimensions and positions are to scale with placements optimized by simulations. Figure from Ref. [49].

A schematic figure of the planned experimental setup is shown in Fig. 4.3. The chosen setup has been designed to optimize detection efficiency. Further details regarding the detectors we are planning to use and their configuration will be provided below.

4.3.2 Detection of protons

Fig. 4.4 shows the kinetic energy of a proton (T_{proton}) versus its hit position along the z-axis (z) for excitation energies of the fissioning nucleus ranging from 6 MeV to 10 MeV (simulated beam energy is 8 MeV/u). GEF predicts a fission barrier of 7.01 MeV for ^{230}Ac. To experimentally determine the value of this barrier unambiguously, it is necessary to register excitation energies at least 2 MeV higher and lower than the predicted barrier. When a compound nucleus with a high excitation energy is formed, the energy of the ejected proton is low. Consequently, the proton has a smaller momentum, also in the direction opposite of the beam. Therefore, it does not travel far in the z direction before completing an orbit in the magnetic field. As shown in the figure, to detect protons ejected from nuclei with high excitation energies, the silicon array should be positioned as close to the target as possible. Due to technical limitations, a distance of about 2 cm from the target is the minimum that can be achieved.

Table 4.1 shows an efficiency of proton detection given that it hits the silicon array for different excitation energies. The distance between the array and target has been set to −20.68 mm and the length of considered array is 350 mm. Most of the emitted protons complete only one single helical orbit before hitting the array (*single-turn protons*). However, there is a certain fraction of protons which have a small energy and a large emission angle with respect to the beam axis, and they complete multiple turns before hitting the silicon array. Such protons are commonly called *multi-turn protons*. In Table 4.1, both single-turn and multi-turn protons have been considered. It can be observed that for higher excitation energies the detection efficiency becomes drastically smaller.

E_x (MeV)	Detection percentage	$\frac{\text{multi-turn protons}}{\text{all detected protons}}$
6	27 %	0.060
7	23 %	0.072
8	19 %	0.10
9	13 %	0.18
10	5.1 %	0.46

Table 4.1: Detection efficiency of protons that hit the silicon array and ratio of detected multi-turn protons to all detected protons for different excitation energies simulated for ^{229}Ac(d,p)^{230}Ac reaction at a beam energy of 8 MeV/u.

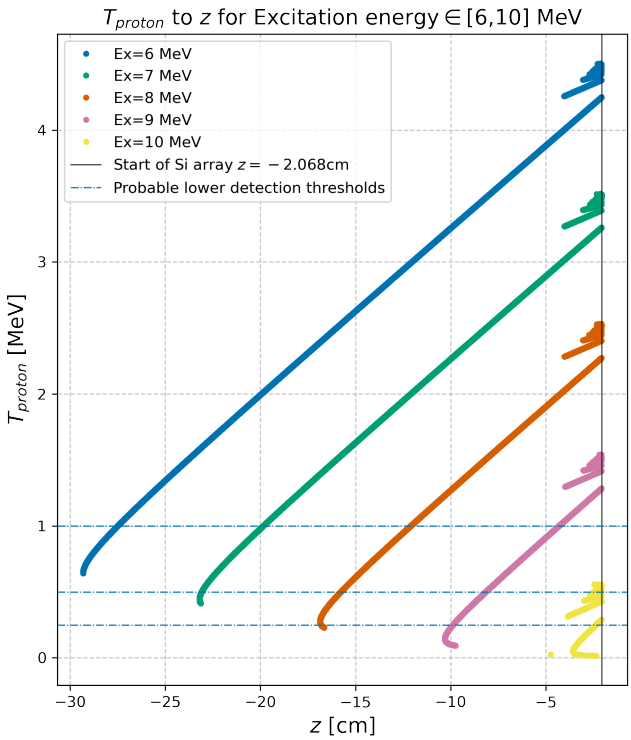

Figure 4.4: Kinetic energy of a proton (T_{proton}) versus its hit position along the z-axis (z) for excitation energies of the fissioning nucleus ranging from 6 MeV to 10 MeV (the simulated beam energy is 8 MeV/u). For each excitation energy, the long line corresponds to protons completing a single turn before hitting the detector, while the shorter lines to the right correspond to multi-turn events. Figure from Ref. [16].

In order to reduce the background of non-proton events, adequate time resolution is essential. We are interested in measuring time interval between detection of fission fragments and detection of a proton in a silicon array. Referring to Eq. (2.2),

$$T_{\mathrm{cyc}} = \frac{2\pi}{B}\frac{m}{Z},$$

we observe that for a proton (with a mass-to-charge ratio $A/Z = 1$) in the magnetic field of strength $B = 2$ T, the cyclotron period is $T_{\mathrm{cyc}} = 32.8$ ns. For a particle with a $A/Z = 2$, such as a deuteron or an alpha particle, the cyclotron period will be twice as long: $T_{\mathrm{cyc}} = 65.6$ ns. The same applies to protons making two turns. Therefore, having time resolution that enables the distinction

between these cases helps to suppress background. Such time resolution capabilities have been demonstrated with the HELIOS silicon array. Fig. 4.5 presents a time-of-flight spectrum for protons emitted from ^{28}Si+$(C_2D_4)_n$ collisions measured with the HELIOS setup [13]. The two peaks are clearly separated.

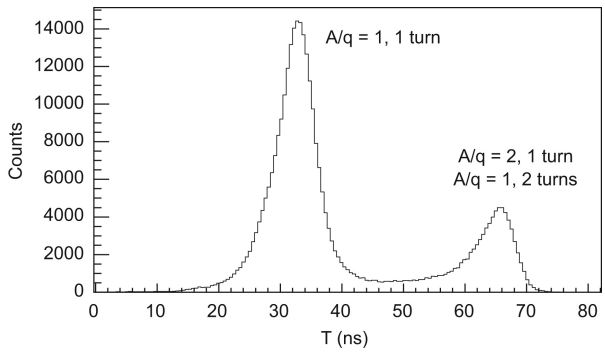

Figure 4.5: Time-of-flight spectrum for protons emitted from ^{28}Si+$(C_2D_4)_n$ collisions measured by the HELIOS setup. Two peaks around 33 ns and 66 ns corresponding to single-orbit protons and alpha particles as well as double-cycle protons can be distinguished. Figure from Ref. [13].

Because we will only consider protons that complete a single turn before depositing energy in the detector, the available statistics will be reduced. The ratio of protons completing multiple turns before hitting the detector to the total number of all detected protons for different excitation energies E_x is presented in Table 4.1. The multi-turn protons constitute an increasingly larger fraction of all events as the E_x increases for a given beam energy. For an energy of 10 MeV, they account for nearly half of all detected protons. Thus, we can expect significantly worse statistics for events with high excitation energy of the fissioning nucleus (where $E_x > 9$ MeV). If time resolution is not sufficient, multi-turn protons can be physically removed by using an obstruction in front of the hollow silicon array, a so-called multi-turn killer. That however is not effective against one-turn alpha particles.

4.3.3 Detection of fission fragments

Figs. 4.6 and 4.7 show results of GEF simulations of ^{230}Ac fission. The two fission fragments are expected to have charges within the range of $30 \leq Z \leq 60$ and masses spanning $80 \leq A \leq 150$. Let us recall the reaction that we intend to study. In the experiment, a ^{229}Ac beam with an energy of 8 MeV/u will impinge on a CD_2 (deuterated plastic) target. There, the (d,p) reaction may occur. The resulting compound ^{230}Ac nucleus will move forward with an energy roughly

similar to the beam. Then, if fission occurs, the fission fragments will move forward within a cone with an opening angle depending on the beam energy and the transverse momentum of the specific fission fragment.

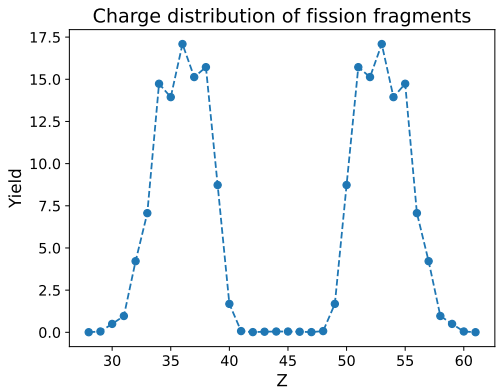

Figure 4.6: Charge distribution of fission fragments for 10^5 events simulated by GEF for ^{230}Ac at an excitation energy $E^* = 7$ MeV above the ground state.

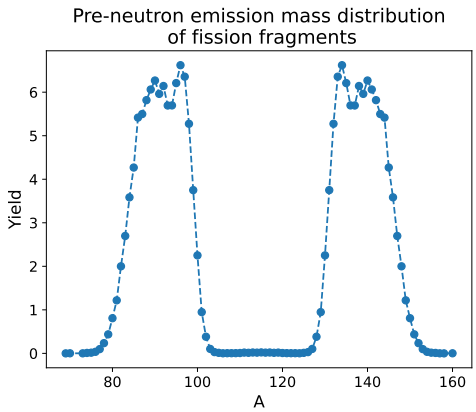

Figure 4.7: Pre-neutron emission mass distribution of fission fragments for 10^5 events simulated by GEF for ^{230}Ac at excitation energy $E^* = 7$ MeV above the ground state.

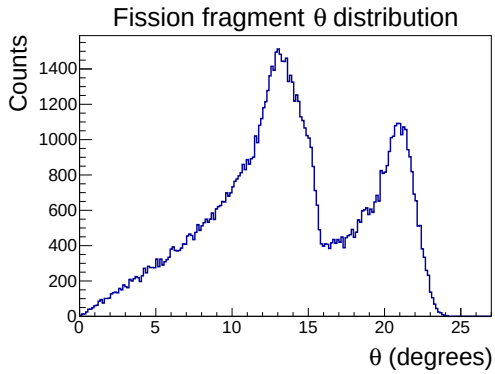

Figure 4.8: Angular distributions of ^{230}Ac fission fragments simulated by GEF and boosted to the beam frame. For the simulated ^{229}Ac beam energy of 8 MeV/u, two peaks around 13° and 21° can be distinguished, corresponding to heavy and light fission fragments, respectively.

Fig. 4.8 shows the angular distribution of fission fragments simulated by GEF and boosted to the beam frame for the planned experiment. Fission fragments are forward-focused.

Due to the kinematics of the emitted fission fragments, the most efficient method for their detection is to employ a CD-shaped[2] detector centered at the beam axis. A hole inside such a detector permits the unreacted beam to pass through. By adjusting its distance from the target, the solid angle covered by the detector can be optimized to maximise the detection efficiency for fission fragments without obstructing trajectories of deuterons (more details on detection of deuterons for background normalisation will be provided in Section 4.3.4).

Fig. 4.9 shows the geometric efficiency of the CD-shaped fission fragment detector with an inner radius of 11 mm and an outer radius of 35 mm used with a beam energy of 8 MeV/u, as a function of its distance from the target. At a distance of 8 cm downstream from the target, the efficiency is 87 % for detecting a single fission fragment and 82 % for detecting both fission fragments in coincidence. This has been chosen as an optimal position for placing the detector.

By using a detector segmented into rings and sectors, it is possible to determine the difference in azimuthal angle between the particles depositing energy in the detector on an event-by-event basis. For fission events, this difference should be 180°, since the fragments are emitted back-to-back in the compound frame, leading to opposite transverse momenta.

[2] *CD* stands for compact disc, a commercial format previously popular for music distribution, developed by Philips and Sony in 1982.

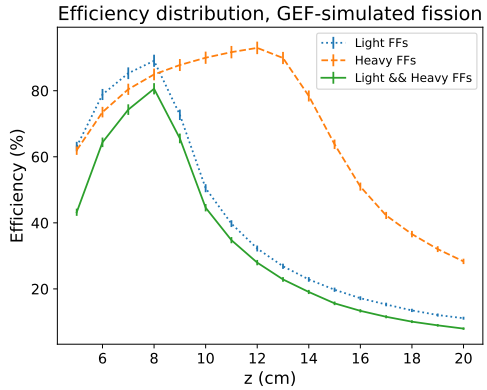

Figure 4.9: Geometric efficiency of the CD-shaped fission fragment detector at a beam energy of 8 MeV/u as a function of its distance to the target. The detector has inner and outer radii of 11 mm and 35 mm, respectively. The dotted blue line represents the efficiency of detecting only the light fission fragment, the dashed orange line corresponds to the efficiency of detecting only the heavy fragment, and the solid green line illustrates the efficiency for detecting both fission fragments in coincidence. Figure from Ref. [50].

Another advantage can be achieved by employing a detector in a ΔE-E configuration. We consider the following setup: a ΔE detector with a thickness of 65 μm positioned in front of a 1000 μm detector. On average, about 39 % of all fragments that reach the ΔE-layer pass through it and reach the E-layer. The expected energy resolution in this setup will not be sufficient to identify the charge and/or mass of the fission fragments. However, lighter nuclei, such as carbon or deuterium nuclei scattered from the target, can be distinguished, in case they reach the detectors. Additionally, it should be still possible to differentiate between light and heavy fragments based on their emission angle as seen in Fig. 4.8.

4.3.4 Detection of deuterons elastically scattered from the target

To extract the fission cross section as a function of excitation energy, it is necessary to know the product of the beam intensity and the number of target particles per unit area. This quantity can be determined using deuteron elastic scattering. By counting such scattered deutrons in a given angular range, it is possible to determine the total fission yield and calculate the cross section. To relate the detected deuterons to the beam intensity and target thickness prod-

uct, the elastic scattering differential cross-section as a function of scattering angle, as well as the scattered deuteron energy for the ejected deuterons in the ^{229}Ac + d reaction have been calculated using the LISE++ program [51] and are shown in Fig. 4.10.

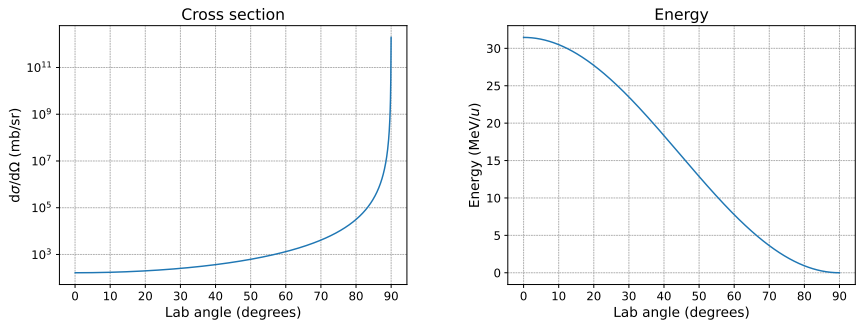

(a) (b)

Figure 4.10: (a) Cross section of deuterons ejected from the target when ^{229}Ac of 8 MeV/u impinges as a function of the lab angle. (b) Energy of the scattered deuterons as a function of the lab angle.

The cross-section noticeably increases for larger angles and reaches infinity at 90°. At the same time, the energy of the deuterons approach 0 MeV for angles close to 90°, while it is at its maximum, reaching about 31 MeV, for small forward angles close to 0°. Deuterons emitted at angles very close to 90°, due to their low energy, will not escape from the target material at all, making their detection impossible. On the other hand, deuterons emitted at angles close to 0°, although highly energetic, are impossible to detect because the beam that did not react moves along the axis of the solenoid and would overlap with such deuterons. Additionally, they are few. Therefore, we need a configuration compromise that ensures the measurement of a sufficient number of deuterons (large angles) with a high enough energy to detect them (forward angles).

The standard configuration used at ISS to detect ejected deuterons consists of an on-axis CD-shaped silicon detector . It is shielded by an aluminium annulus and a tube passing through the centre of the annulus as shown in Fig. 4.11. Consequently, particles can only access the detector by passing around outside the shield. Thus, only deuterons emitted within a narrow range of angles can be detected. The distance between the detector and the target can be changed which results in the detection of deuterons emitted at different angles.

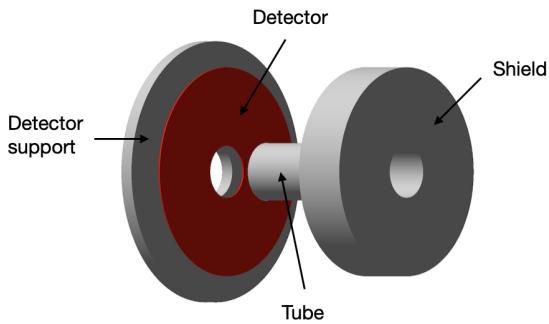

Figure 4.11: Schematic of the standard luminosity detection setup for elastically scattered deuterons used at ISS (not to scale). The tube is normally inside the detector, leaving no gap. The detector inner and outer radii are 24 mm and 48 mm, respectively.

Fig. 4.12 shows a configuration for which the luminosity detector is placed 12.5 cm from the target, and the fission fragment detector 18 cm from the target. Example trajectories of detected deuterons are represented as well as a few example trajectories of the light and heavy fission fragments. As seen in Fig. 4.12, placing the standard detector configuration in front of the fission fragment detector is not possible — the fission fragments would then collide with the luminosity detector. On the other hand, if we place the luminosity detector behind the fission fragment detectors, it is possible to detect deuterons without disturbing the trajectories of the fission fragments (see Fig. 4.13). However, in such a configuration, only deuterons emitted at smaller laboratory scattering angles could be detected (with a smaller cross-section). A maximum efficiency of 0.36 % for all emitted deuterons for this setup can be obtained when optimising the position of the luminosity detector. With the expected beam intensity, it might result in insufficient statistics.

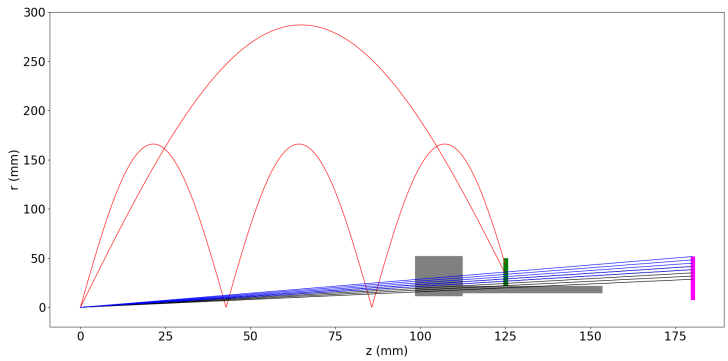

Figure 4.12: Schematic illustration of particle trajectories in the luminosity detection setup. The luminosity detector is shown in green, the shield and tube in gray, and the fission fragment detector (just one is shown) in magenta. Example trajectories of detected deuterons are represented as red lines, while a few example trajectories of the light and heavy fission fragments are shown as blue and black lines, respectively. In this configuration, the fission fragment detector is obscured. The ordinate shows the transverse distance from the beam axis, r, while the abscissa is the distance along the beam axis, z.

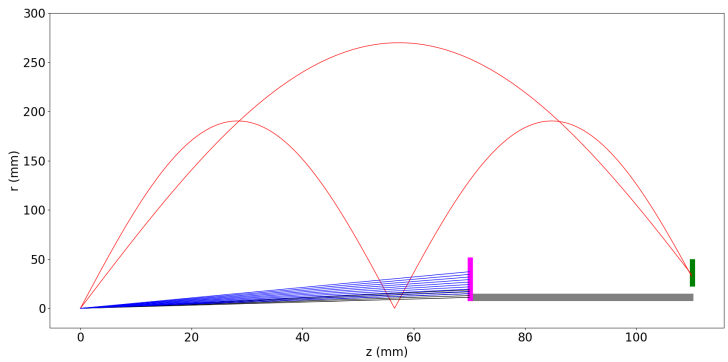

Figure 4.13: Similar to Fig. 4.12, but with the fission fragment detector (just one is shown) placed in-between the luminosity detector and the target. Note: helical trajectories circulating around (x, y) passing through $(x, y) = (0, 0)$ and progressing in the z direction look like bouncing balls when projected onto an r-z-plane.

To address this issue, an alternative off-axis configuration has been proposed using four position-sensitive silicon detectors, as illustrated in Fig. 4.3. In this setup, the efficiency for detecting elastically scattered deuterons reaches 0.8 % for detectors mounted parallel to the beam-line, with the active surface of 5 cm^2 oriented such that they face the beam axis, positioned 2 cm downstream from the target and 3 cm off the beam axis. The efficiency map for such a luminosity detector configuration, as a function of the off-axis distance and target distance parallel to the beam axis, is shown in Fig. 4.14. The efficiency is the highest when the detectors are placed close to the target. However, placing them as close as possible to the target is not feasible due to the presence of other detectors and the potential blocking of other particles that need to be detected, as well as transverse movements of the target holding structure itself.

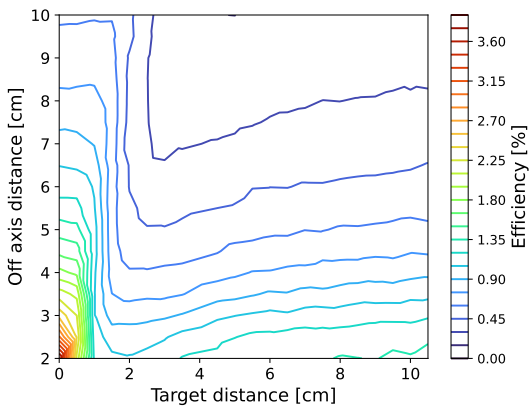

Figure 4.14: Efficiency map for a luminosity detector consisting of four position-sensitive silicon detectors mounted parallel to the beam-line, with the active surface oriented such that they face the beam axis, as a function of the off-axis distance and distance to the target plane. Figure from Ref. [50].

4.3.5 Detection of γ rays

A measurement of γ-rays is planned to acquire data on the total energy and multiplicity of γ-rays emitted during fission. This is valuable for *r-process* simulations and could contribute to a better understanding of angular momentum generation in fission [48].

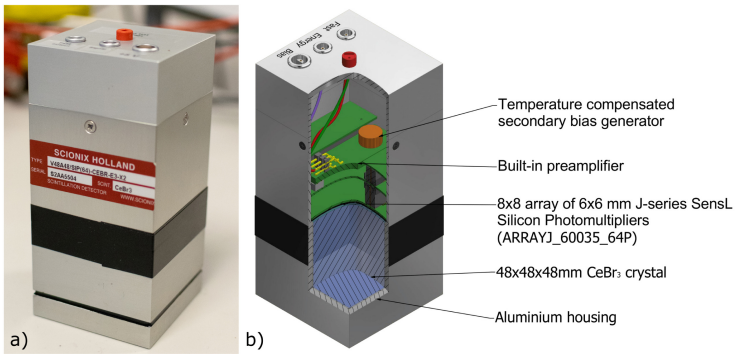

Figure 4.15: a) A single SpecMAT scintillation detector. b) The inner structure of the detector (CAD drawing). Figure from Ref. [52].

Detecting γ-rays in coincidence with (d,pf) reactions requires the use of γ-ray detectors inside the vacuum vessel and in a strong magnetic field. The measurement will be conducted using the $CeBr_3$ crystals from the SpecMAT detector [52], designed by the KU Leuven group. SpecMAT is an active target, and in the initial design, the $CeBr_3$ scintillation detectors are placed in a cylindrical configuration around the active target. However, the $CeBr_3$ detectors can also be used separately, and for this purpose, a new mechanical holder has been constructed in which the crystals are arranged in 11 spikes, with three crystals per spike, as shown in Fig. 4.16. In the subsequent part of the text, this spike configuration will be referred to as the *original SpecMAT configuration*.

Each detector unit consists of a $48 \times 48 \times 48$ mm^3 $CeBr_3$ crystal placed inside an aluminium housing. The aluminum housing has a thickness of 1 mm on the side facing the γ-ray window and 3 mm on the side walls. A single detector and its inner structure is shown in Fig. 4.15.

The original scintillation array design consists of 11 spokes of 3 crystals, 33 crystals in total, and is shown in Fig. 4.16. The detector array centre is positioned 150 mm downstream from the target.

The SpecMAT scintillation array achieves a γ detection efficiency of 2.5 % at an energy of 1 MeV [53].

The initial geometry of the scintillator array has been optimized as part of this thesis work to maximise the total energy and multiplicity detection efficiency. More details about the simulations are provided in Section 4.3.7.

4.3.6 Experimental challenges

Executing this experiment will be challenging for several reasons. Firstly, we are limited by the energies available at HIE-ISOLDE (maximum 8 MeV/u at the time of writing this text) and the beam intensities available (maximum

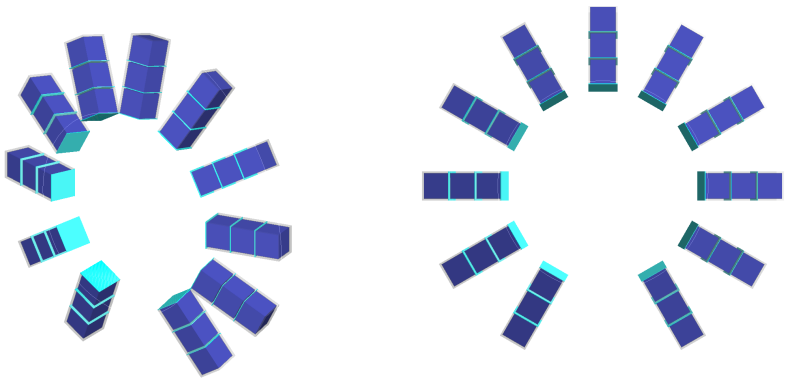

(a) (b)

Figure 4.16: The original SpecMAT configuration (11 spokes of 3 crystals). (a) Side view. (b) Face view.

$1.3{\times}10^7$ pps expected for ^{229}Ac from the primary ISOLDE target). Additionally, the transmission coefficient from the primary target through ISOLDE—HIE-ISOLDE to the experimental ISS target is estimated to be 1% for such a heavy element.

A second challenge lies in the low cross sections for the (d,p) and (d,pf) reactions. The GEF model predicts the total fission probability of ^{230}Ac as $P_f = 3$ % compared to 20 % for ^{239}U. Prediction of the (d,p) cross section is challenging because the structure of ^{230}Ac is not sufficiently well studied and because many unknown levels are expected to contribute to the cross section. Therefore, we assume that the (d,p) cross section does not change significantly between ^{229}Ac and ^{238}U.

Another challenge are beam impurities. In the case of the planned experiment, the most troublesome contaminants will be isotopes with a higher fission probability and a lower fission barrier. According to the predictions of the GEF model, for isotopes with similar A/q, isotopes with atomic numbers $Z \geq 89$ have a significantly higher fission probability. However, on the other hand, impurities with $Z \leq 89$ will not pose a problem. Based on estimates by the ISOLDE source group, only minor impurities with $Z \leq 89$ can be expected during the experiment.

4.3.7 Gamma array simulations

In this section, simulations performed to find the optimal γ array arrangement are presented.

We are interested in the total energy emitted from the fission fragments (not

single γ lines). Thus, our primary concern would be a detector covering as large a solid angle as possible.

Three types of geometries have been considered:

- a box with 3 rings (12 crystals in each ring, for a total of 36),
- a box with 2 rings (16 crystals in each ring, for a total of 32),
- original SpecMAT (11 spokes of 3 crystals, for a total of 33).

Two different cases are considered for the box configurations: with and without overlap. The box with overlap aims to avoid γ rays escaping in the detector corners. The idea is that a box γ array would be placed downstream just behind the target. Visualisations of the considered geometries are presented in Figs. 4.16 to 4.18.

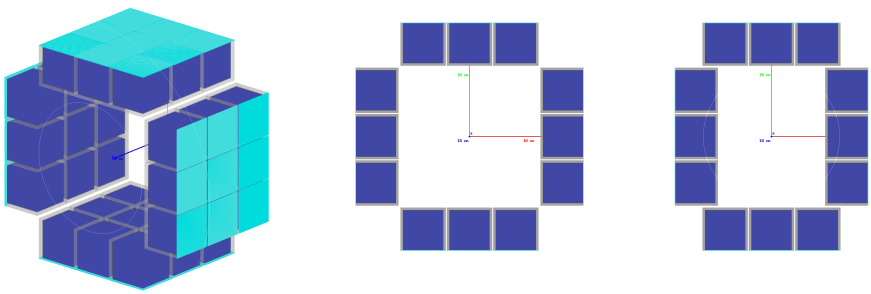

(a) (b) (c)

Figure 4.17: Box with 3 rings (12 crystals in each ring, for a total of 36). (a) Without overlap, side view. (b) Without overlap, face view. (c) With overlap, face view.

When a γ interacts with matter, it may deposit part of its energy in one detector crystal and the scattered photon can then travel to one or several other crystals. Then the total energy of the γ would then be the sum of the energies deposited in all crystals it interacted with. Addback is an analysis method to sum these energies together. However, it may also incorrectly sum contributions that did not result from a common original photon.

As a first approximation we consider two fission fragments moving downstream from the target, and one of them is emitting a single γ with an energy between 0 and 10 MeV. How many events would we see in our detector?

For that a simple check has been prepared using the simplest addback possible — adding the energies detected in all crystals. Table 4.2 presents the

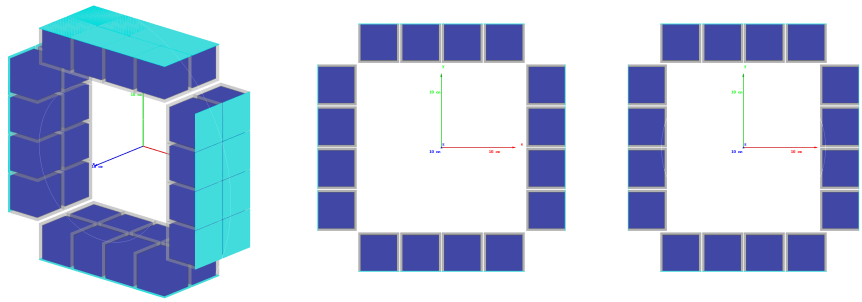

(a) (b) (c)

Figure 4.18: Box with 2 rings (16 crystals in each ring, for a total of 32). (a) Without overlap, side view. (b) Without overlap, face view. (c) With overlap, face view.

fraction of detected events for each considered geometry, the fraction of fully registered events (registered energy above 99 % of the original energy), the fraction of incompletely registered events (registered energy between 1 % and 99 % of the original energy), and the ratio of incomplete to fully registered events.

Note that the given numbers correspond to detected events of any energy so it is more like a geometric efficiency and it is assumed that no Doppler correction is needed.

Geometry	Fraction of detected events	Fraction of fully registered events (> 99 %)	Fraction of incompletely registered events (1 % $- 99$ %)	Ratio of incomplete to complete events
org. SpecMAT	0.045	0.0095	0.035	3.61
Box (3 rings, no overlap)	0.23	0.05	0.18	3.43
Box (3 rings, overlap)	0.24	0.06	0.18	3.28
Box (2 rings, no overlap)	0.145	0.032	0.113	3.50
Box (2 rings, overlap)	0.15	0.03	0.12	3.38

Table 4.2: Detection efficiency for different configurations (one γ emitted from one fission fragment). All fractions are relative to the number of original γ photons. Due to other geometric constraints, the 2 ring box configuration with a photopeak efficiency of 3 % is chosen.

Unsurprisingly, the 3-ring box configuration would be the most efficient. However various geometrical constraints of the setup also need to be considered:

Each crystal is 48 mm×48 mm×48 mm. In the case of the 3-ring geometry, the γ array would extend to +15 cm in the z-direction. Also, the inner dimension of the array would be about 15 cm (or about 14 cm if using the configuration with overlap). For fission fragments detection, as mentioned before, two CD-shaped segmented silicon detectors with a diameter of about 14 cm (active area + PCB support) will be used. According to the simulations, the fission fragment detector should be placed 8 cm from the target, thus inside the γ array. Considering that, the 3-ring geometry is not feasible (too tight inner dimension).

With the 2-ring geometry, the inner dimension gives enough space to fit the CD-shaped detectors (as well as off-axis luminosity detectors close to the target).

The results of the above simulations in terms of the fraction of energy detected are presented graphically in Fig. 4.19 for SpecMAT and a box with 2 rings. The plots show all events sorted by their reconstruction efficiency.

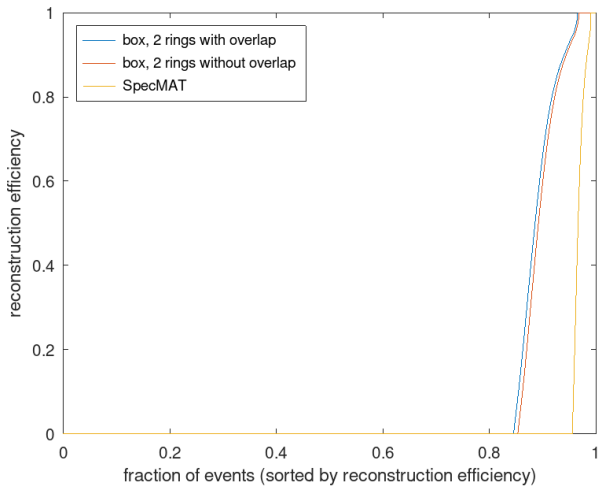

(a)

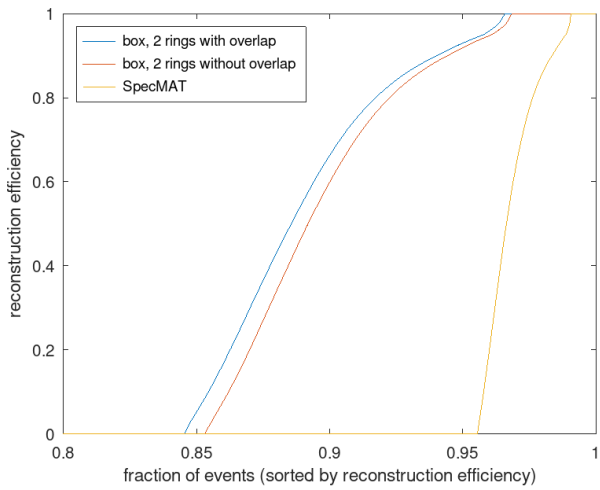

(b)

Figure 4.19: Detection efficiency for different configurations. The efficiency is calculated for each event as the registered energy divided by the originally emitted γ energy. The events are then sorted by efficiency. The left plot shows all events. On the right, the region with non-zero energy deposits is shown.

Ideally, we would be interested in a geometry for which there is a long plateau around 1 (many γ rays fully detected).

The performance of different configurations is also compared using Doppler-corrected spectra, see Fig. 4.20. The following rules are used:

1. only neighbours at most 2 crystals away are included in each cluster, i.e. contributiong to addback,

2. the γ ray direction is an energy-weighted average of the included crystal positions,

3. the Doppler correction uses the beam velocity and nominal direction (since it is not known from which fission fragment the γ was emitted).

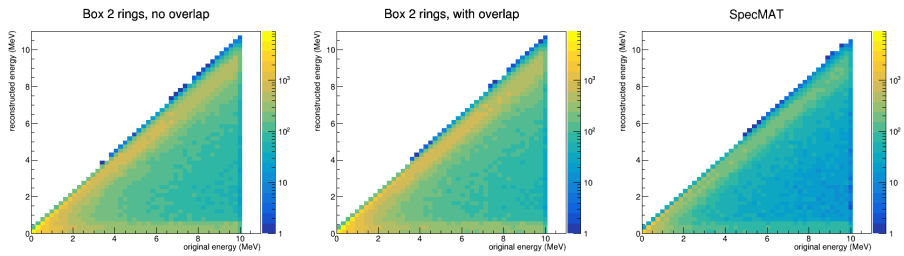

Figure 4.20: Doppler-corrected vs simulated γ energy for a box with 2 rings without and with overlap, and SpecMAT. Except for the total efficiency differences between the configurations, the Doppler-corrected energies look very similar.

During support design, the chosen design was modified to an overlap design but with four crystals above and below and five at each side in each ring. This allows for a tight configuration, with the same vertical and horizontal inner dimension.

Chapter 5

Summary and outlook

Studying fission of neutron-rich nuclei is very interesting for several reasons. First of all, the fission barrier heights of neutron-rich actinides provide an important input to theoretical models investigating the r-process. Moreover, the analysis of the total energy of γ rays emitted by fission fragments allows for estimating the total energy available in the fissioning system, while data on the multiplicity of γ rays enables a better understanding of the angular momentum generation of the two fission fragments. However, due to technical difficulties, the region of neutron-rich isotopes, especially actinides, has so far remained unexplored, and the fission properties of these elements are generally unknown.

To address this issue, a new experimental technique, namely light-ion transfer in inverse kinematics, has been developed. The applicability of this technique has been tested in a pilot fission experiment conducted at ANL. The experimental details, as well as data analysis, have been presented in Chapter 3. The results show that it is possible to extract the fission barrier height using a (d,pf) reaction in a magnetic field. Therefore, preparations are underway for a similar experiment, this time using a radioactive beam.

In Chapter 4, simulations and plans for the future IS739 experiment studying the fission of ^{230}Ac have been presented. The IS739 setup has been optimised for the detection of fission events. This required selecting the most optimal type and size of a detector for fission fragments from those available on the market and optimizing its distance from the target, as well as optimizing the position of the existing silicon array for proton detection. A similar optimization procedure was also carried out for luminosity detectors, which are detectors measuring deuterons elastically scattered from the target for beam normalization.

For the detection of emitted gamma rays, 36 scintillation detectors will be used. Simulations have been conducted to determine their optimal positions for the detection of as much as possible of the total energy. Mechanical support is being manufactured and will be ready to use in the IS739 experiment. It has

been demonstrated that reconstruction of the total γ energy (and multiplicity) is possible with an unfolding procedure [54]. For the future data analysis, a similar kind of algorithm is planned to be implemented.

The experiment proposal has been accepted by the ISOLDE committee (INTC). Beam time for this experiment has been requested for the summer or autumn of 2024. This will be the first experiment investigating the fission of a neutron-rich isotope in inverse kinematics, allowing for the determination of the fission barrier height for an element currently lacking such experimental data.

Appendix A

Kinematics of two-body scattering

We want to describe a scattering process, where a projectile particle **a** of mass m_a with kinetic energy T collides with a target particle **b** of mass m_b. After scattering, the particles **1** and **2** of masses m_1 and m_2, respectively, emerge, as shown in Fig. A.1. In this particular case, the center of mass of the system is connected with the laboratory reference frame through a Lorentz boost with velocity $\vec{v} = \vec{\beta}c$.

In general, given four quantities A and $\mathbf{Z} = (Z_X, Z_Y, Z_Z)$ in a reference system S and their counterparts A' and $\mathbf{Z}' = (Z'_X, Z'_Y, Z'_Z)$ in a Lorentz-boosted reference system S', the Lorentz transformation acts as:

$$\begin{aligned} A' &= \gamma\left(A - \frac{v\hat{n}\cdot\mathbf{Z}}{c}\right), \\ \mathbf{Z}' &= \mathbf{Z} + (\gamma-1)(\mathbf{Z}\cdot\hat{n})\hat{n} - \frac{\gamma A v\hat{n}}{c}, \end{aligned} \tag{A.1}$$

where $\hat{n}$ is the direction of relative motion between S and S' of velocity $\vec{v} = v\hat{n}$, $\hat{\beta} \parallel \hat{n}$, and $\gamma = \frac{1}{\sqrt{1-\beta^2}}$.

Putting $A \to E$ and $\mathbf{Z} = (Z_X, Z_Y, Z_Z) \to \vec{k}$, where E is the total energy and $\vec{k}$ is the momentum vector, θ is the angle between $\vec{\beta}$ and $\vec{k}$, and $\hat{\beta} \perp \hat{l}$, the four-momentum vector $\mathbb{P}$ transforms to $\mathbb{P}'$ as:

$$\begin{aligned} \mathbb{P} = \begin{pmatrix} E \\ \vec{k} \end{pmatrix} \to \mathbb{P}' = \begin{pmatrix} E' \\ \vec{k}' \end{pmatrix} &= \begin{pmatrix} \gamma E - \gamma\vec{\beta}\cdot\vec{k} \\ \vec{k} + (\gamma-1)(\vec{k}\cdot\hat{\beta})\hat{\beta} - \gamma E\vec{\beta} \end{pmatrix} \\ &= \begin{pmatrix} \gamma E - \gamma\beta k\cos\theta \\ (-\gamma E\beta + \gamma k\cos\theta)\hat{\beta} + k\sin\theta\,\hat{l} \end{pmatrix} \end{aligned} \tag{A.2}$$

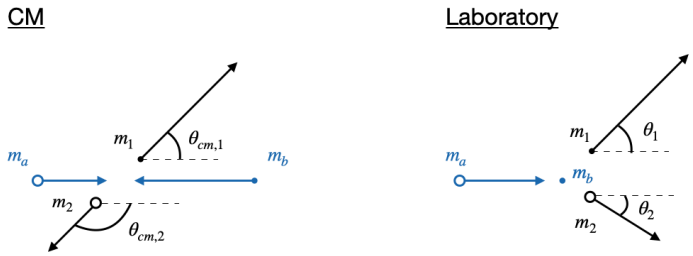

Figure A.1: 2-body scattering in the center of mass (CM) frame (on the left) and in the laboratory frame (on the right). a and b label the particles before the interaction while 1 and 2 are the emerging particles.

Let us return to the scattering process. Working with $c = 1$, the initial four-momenta of particles a and b in the lab frame are:

$$\mathbb{P}_\mathrm{a} = \begin{pmatrix} E_\mathrm{a} \\ \vec{k}_\mathrm{a} \end{pmatrix} = \begin{pmatrix} \sqrt{m_\mathrm{a}^2 + k_\mathrm{a}^2} \\ \vec{k}_\mathrm{a} \end{pmatrix}, \qquad \mathbb{P}_\mathrm{b} = \begin{pmatrix} m_\mathrm{b} \\ \vec{0} \end{pmatrix}, \tag{A.3}$$

where $\mathbf{k}_\mathrm{a}$ is the initial momentum of particle a in the lab frame.

The four-vector of the center of mass of the system as seen in the laboratory frame can be expressed as:

$$\mathbb{P}_\mathrm{c} = \mathbb{P}_\mathrm{a} + \mathbb{P}_\mathrm{b} = \begin{pmatrix} \sqrt{m_\mathrm{a}^2 + k_\mathrm{a}^2} + m_\mathrm{b} \\ \vec{k}_\mathrm{a} \end{pmatrix} = \begin{pmatrix} E_\mathrm{c} \\ \vec{k}_\mathrm{a} \end{pmatrix}. \tag{A.4}$$

The frame-independent energy-momentum relation for the system is:

$$\begin{aligned} M_\mathrm{c}^2 &= E_\mathrm{c}^2 - k_\mathrm{a}^2, \\ M_\mathrm{c}^2 &= m_\mathrm{a}^2 + k_\mathrm{a}^2 + 2m_\mathrm{b}\sqrt{m_\mathrm{a}^2 + k_\mathrm{a}^2} + m_\mathrm{b}^2 - k_\mathrm{a}^2, \\ M_\mathrm{c} &= \sqrt{m_\mathrm{a}^2 + m_\mathrm{b}^2 + 2m_\mathrm{b}\sqrt{m_\mathrm{a}^2 + k_\mathrm{a}^2}}, \end{aligned} \tag{A.5}$$

where M_c is total invariant mass of the system.

We know that in the general case, for a particle with rest mass m_0 and velocity $\vec{\beta}$, the following relations apply:

$$\begin{aligned} \vec{p} &= \gamma m_0 \vec{v}, \\ p &= \gamma m_0 \beta c, \\ p^2 &= \gamma^2 m_0^2 \beta^2 c^2. \end{aligned} \tag{A.6}$$

Letting $c \to 1$, $\vec{p} \to \vec{k_{\mathrm{a}}}$, $m_0 \to M_{\mathrm{c}}$, and then using $E_{\mathrm{c}} \to \gamma M_{\mathrm{c}}$, we get:

$$\begin{aligned} \vec{k_{\mathrm{a}}}^{\,2} &= \gamma^2 M_{\mathrm{c}}^2 \beta^2, \\ \vec{k_{\mathrm{a}}}^{\,2} &= E_{\mathrm{c}}^2 \beta^2, \\ \vec{\beta} = \frac{\vec{k_{\mathrm{a}}}}{E_{\mathrm{c}}}, &\quad \gamma\vec{\beta} = \frac{\vec{k_{\mathrm{a}}}}{M_{\mathrm{c}}}. \end{aligned} \tag{A.7}$$

We change view to the CM by applying the Lorentz transformation:

$$\mathbb{P}'_{\mathrm{c}} = \begin{pmatrix} \gamma E_{\mathrm{c}} - \gamma\vec{\beta} \cdot \vec{k_{\mathrm{a}}} \\ \vec{k_{\mathrm{a}}} + (\gamma - 1)(\vec{k_{\mathrm{a}}} \cdot \hat{\beta})\hat{\beta} - \gamma\vec{\beta}E_{\mathrm{c}} \end{pmatrix} \tag{A.8}$$

After using Eq. (A.5), Eq. (A.7), and the fact that $\vec{\beta} \parallel \vec{k_{\mathrm{a}}}$, so that $(\vec{k_{\mathrm{a}}} \cdot \hat{\beta})\hat{\beta} = \vec{k_{\mathrm{a}}}$, we obtain:

$$\mathbb{P}'_{\mathrm{c}} = \begin{pmatrix} M_{\mathrm{c}} \\ \vec{0} \end{pmatrix}. \tag{A.9}$$

$\mathbb{P}_a$ and $\mathbb{P}_b$ in the center-of-mass frame are obtained in the same way by applying Lorentz transformations:

$$\mathbb{P}'_{\mathrm{a}} = \begin{pmatrix} \gamma\sqrt{m_{\mathrm{a}}^2 + k_{\mathrm{a}}^2} - \gamma\vec{\beta} \cdot \vec{k_{\mathrm{a}}} \\ -\gamma\vec{\beta}\sqrt{m_{\mathrm{a}}^2 + k_{\mathrm{a}}^2} + \gamma\vec{k_{\mathrm{a}}} \end{pmatrix}, \tag{A.10}$$

$$\mathbb{P}'_{\mathrm{b}} = \begin{pmatrix} \gamma m_{\mathrm{b}} \\ -\gamma\vec{\beta}m_{\mathrm{b}} \end{pmatrix}. \tag{A.11}$$

The scattered particles can be described by four-vectors in the center-of-mass frame:

$$\mathbb{P}'_1 = \begin{pmatrix} \sqrt{m_1^2 + p^2} \\ \vec{p} \end{pmatrix}, \qquad \mathbb{P}'_2 = \begin{pmatrix} \sqrt{m_2^2 + p^2} \\ -\vec{p} \end{pmatrix}. \tag{A.12}$$

The energies of particles 1 and 2 are:

$$\begin{aligned} q &= \sqrt{m_1^2 + p^2}, \\ Q &= \sqrt{m_2^2 + p^2}. \end{aligned} \tag{A.13}$$

The total energy in the CM frame, E_{t}, can be expressed as:

$$E_{\mathrm{t}} = q + Q, \tag{A.14}$$

After solving this for q, we obtain:

$$q = \frac{E_{\mathrm{t}}^2 - m_2^2 + m_1^2}{2E_{\mathrm{t}}}. \tag{A.15}$$

In a similar way, we can calculate Q:

$$Q = \frac{E_{\mathrm{t}}^2 + m_2^2 - m_1^2}{2E_{\mathrm{t}}}. \tag{A.16}$$

Let us return to our 4-vectors (Eq. (A.12)). We return to the laboratory frame using the inverse Lorentz transformation:

$$\begin{aligned} \mathbb{P}_1 &= \begin{pmatrix} \gamma\sqrt{m_1^2 + p^2} + \gamma\vec{\beta}\cdot\vec{p} \\ \gamma\sqrt{m_1^2 + p^2}\vec{\beta} + \vec{p} + (\gamma - 1)(\hat{\beta}\cdot\vec{p})\hat{\beta} \end{pmatrix}, \\ \mathbb{P}_2 &= \begin{pmatrix} \gamma\sqrt{m_2^2 + p^2} - \gamma\vec{\beta}\cdot\vec{p} \\ \gamma\sqrt{m_2^2 + p^2}\vec{\beta} - \vec{p} - (\gamma - 1)(\hat{\beta}\cdot\vec{p})\hat{\beta} \end{pmatrix}. \end{aligned} \tag{A.17}$$

The particles 1 and 2 are scattered to angles $\theta_{\mathrm{cm},1}$ and $\theta_{\mathrm{cm},2}$ in the CM frame, respectively. We know that $\theta_{\mathrm{cm},2} = \pi - \theta_{\mathrm{cm},1}$. The momentum parts can be rewritten using $\hat{\beta}\cdot\vec{p} = p\cos\theta_{\mathrm{cm},1}$ for particle 1 and $\hat{\beta}\cdot\vec{p} = p\cos\theta_{\mathrm{cm},2} = -p\cos\theta_{\mathrm{cm},1}$ for particle 2:

$$\begin{aligned} \mathbb{P}_1 &= \begin{pmatrix} \gamma\sqrt{m_1^2 + p^2} + \gamma\beta p\cos\theta_{\mathrm{cm},1} \\ \left(\gamma\beta\sqrt{m_1^2 + p^2} + \gamma p\cos\theta_{\mathrm{cm},1}\right)\hat{\beta} + p\ \sin\theta_{\mathrm{cm},1}\ \hat{l} \end{pmatrix}, \\ \mathbb{P}_2 &= \begin{pmatrix} \gamma\sqrt{m_2^2 + p^2} + \gamma\beta p\cos\theta_{\mathrm{cm},1} \\ \left(\gamma\beta\sqrt{m_2^2 + p^2} + \gamma p\cos\theta_{\mathrm{cm},1}\right)\hat{\beta} + p\ \sin\theta_{\mathrm{cm},1}\ \hat{l} \end{pmatrix}, \end{aligned} \tag{A.18}$$

where $\hat{\beta} \perp \hat{n}$.

The four-momenta of particles 1 and 2 in the lab frame can be rewritten as:

$$\begin{aligned} \mathbb{P}_1 &= \begin{pmatrix} E \\ p_z \\ p_{xy} \end{pmatrix} = \begin{pmatrix} \gamma q + \gamma\beta p\cos\theta_{\mathrm{cm},1} \\ \gamma\beta q + \gamma p\cos\theta_{\mathrm{cm},1} \\ p\sin\theta_{\mathrm{cm},1} \end{pmatrix} = \begin{pmatrix} E \\ k\cos\theta_1 \\ k\sin\theta_1 \end{pmatrix}, \\ \mathbb{P}_2 &= \begin{pmatrix} E' \\ p'_z \\ p'_{xy} \end{pmatrix} = \begin{pmatrix} \gamma Q + \gamma\beta p\cos\theta_{\mathrm{cm},1} \\ \gamma\beta Q + \gamma p\cos\theta_{\mathrm{cm},1} \\ p\sin\theta_{\mathrm{cm},1} \end{pmatrix} = \begin{pmatrix} E' \\ k'\cos\theta_2 \\ k'\sin\theta_2 \end{pmatrix}, \end{aligned} \tag{A.19}$$

where $\theta_{\mathrm{cm},1}$ and $\theta_{\mathrm{cm},2}$ are the center of mass scattering angle of particles 1 and 2, k and k' are the momenta of particles 1 and 2 in the lab frame, and θ_1 and θ_2 are the scattering angles in the lab frame of particles 1 and 2.

Appendix B

Finite axial detector

A finite axial detector is a polygonal prism centered along the spectrometer axis and enveloping it, surpassing the transverse beam size. A schematic representation of a finite axial detector is shown in Fig. B.1. The projection of the particle trajectory onto the xy plane is depicted as a blue circle, and one of the detector planes is illustrated as an orange line.

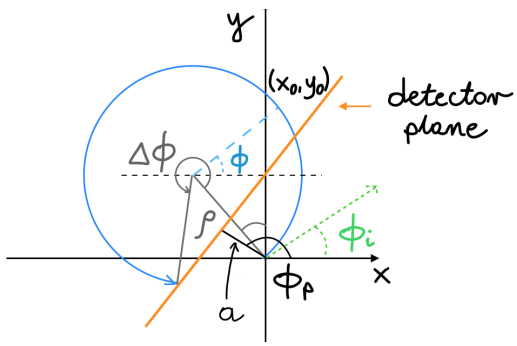

Figure B.1: A schematic representation of a particle trajectory projected onto the xy plane is depicted as a blue circle, while the detector plane is represented by an orange line. ϕ_i denotes the initial emission angle of the particle, and ϕ_p is the angle between the normal of a detector plane and the x-axis. Additionally, a represents the shortest distance between the detector plane and the center of the detector prism, and ρ is the particle trajectory bending radius.

To analyse the particle impact position on the detector, we begin by observing that the normal of the detector plane is:

$$\hat{n} = (\cos\phi_\mathrm{p}, \sin\phi_\mathrm{p}, 0)\,. \tag{B.1}$$

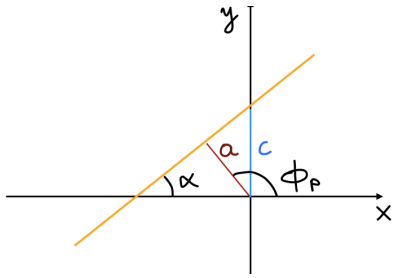

Figure B.2: The detector plane in detail. ϕ_p is the angle between the normal of a detector plane and the x-axis, a is the shortest distance between the plane and the center of the detector, c is the intercept at the y axis, and α is a helper angle.

Let us consider the equation for the detector plane which is shown in Fig. B.2.

A simple formula for the detector plane:

$$y = bx + c, \tag{B.2a}$$

$$b = \tan\alpha = \tan\left(\pi - \left(\frac{\pi}{2} - \phi_\mathrm{p}\right)\right) = -\frac{1}{\tan\phi_\mathrm{p}}, \tag{B.2b}$$

$$y = -\frac{\cos\phi_\mathrm{p}}{\sin\phi_\mathrm{p}}x + c, \tag{B.2c}$$

$$a = c\sin\phi_\mathrm{p}. \tag{B.2d}$$

After transformation:

$$x\cos\phi_\mathrm{p} + y\sin\phi_\mathrm{p} = a. \tag{B.3}$$

The equation describing the trajectory of a positively charged particle in the magnetic field aligned along the z-axis is:

$$\begin{pmatrix} x \\ y \end{pmatrix} = \begin{pmatrix} x_0 + \rho\cos\phi \\ y_0 + \rho\sin\phi \end{pmatrix}, \tag{B.4}$$

where (x_0, y_0) is the center of the particle trajectory in the xy plane and ϕ changes as the particle moves. (x_0, y_0) can be expressed as:

$$\begin{cases} x_0 = -\rho\sin\phi_i, \\ y_0 = \rho\cos\phi_i. \end{cases} \tag{B.5}$$

where ϕ_i is the initial ϕ angle of the emitted particle.

A charged particle in the magnetic field undergoes revolutions in the xy plane. Consequently, the angle ϕ continually varies, and the transverse (v_{xy}) and longitudinal (v_z) velocity components of the particle are:

$$\begin{cases} v_{\mathrm{z}} = v\cos\theta = \frac{z}{t}, \\ v_{\mathrm{xy}} = v\sin\theta = \omega\rho = \frac{\phi}{t}\rho, \end{cases} \tag{B.6}$$

where ω is an angular frequency, t is the time of flight of the particle returning to the solenoid axis, and θ is the initial polar angle of the particle. From that we get:

$$\phi = \tan\theta \cdot \frac{z}{\rho}. \tag{B.7}$$

Initially, at $\phi = \phi_0$, ϕ is shifted relative to the initial angle by $\phi_0 = -\left(\frac{\pi}{2} - \phi_i\right) = \phi_i - \frac{\pi}{2}$:

$$\begin{pmatrix} x \\ y \end{pmatrix} = \rho \begin{pmatrix} -\sin\phi_i + \sin\left(\tan\theta \cdot \frac{z}{\rho} + \phi_i\right) \\ \cos\phi_i - \cos\left(\tan\theta \cdot \frac{z}{\rho} + \phi_i\right) \end{pmatrix}. \tag{B.8}$$

We want to find the z-coordinates of the hit point z_{hit}. After inserting Eq. (B.8) into Eq. (B.3) and doing some algebraic manipulation:

$$\tan\theta \cdot \frac{z_{\mathrm{hit}}}{\rho} = \phi_{\mathrm{p}} - \phi_i + \arcsin\left(\frac{a}{\rho} + \sin\left(\phi_i - \phi_{\mathrm{p}}\right)\right). \tag{B.9}$$

The particle can cross the virtual detector plane n times. We use the formula:

$$\sin\left(x + n\pi\right) = (-1)^n \sin\left(x\right), \tag{B.10}$$

and obtain:

$$z_{\mathrm{hit}} = \frac{\rho}{\tan\theta}\left(\phi_{\mathrm{p}} - \phi_i + n\pi + (-1)^n \arcsin\left(\frac{a}{\rho} + \sin\left(\phi_i - \phi_{\mathrm{p}}\right)\right)\right). \tag{B.11}$$

We need to exclude hit-points from the inside of the detector (not physically possible). The direction vector of the particle is (from differentiating Eq. (B.8)):

$$\frac{\mathrm{d}}{\mathrm{d}z}\begin{pmatrix} x \\ y \end{pmatrix} = \tan\theta \begin{pmatrix} \cos\left(\tan\theta \cdot \frac{z}{\rho} + \phi_i\right) \\ \sin\left(\tan\theta \cdot \frac{z}{\rho} + \phi_i\right) \end{pmatrix}. \tag{B.12}$$

When the particle hits the detector from the outside, the angle between the detector plane normal and the direction of the particle is in the range $\theta' \in \left(\frac{\pi}{2}, \frac{3\pi}{2}\right)$ i.e. the dot product of the direction vector with the detector plane normal is less than 0:

$$\hat{n} \cdot \frac{\mathrm{d}}{\mathrm{d}z}\begin{pmatrix} x \\ y \end{pmatrix} = |n| \cdot \left| \frac{\mathrm{d}}{\mathrm{d}z}\begin{pmatrix} x \\ y \end{pmatrix} \right| \cdot \cos\theta' < 0, \tag{B.13}$$

$$\begin{aligned} \hat{n} \cdot \frac{\mathrm{d}}{\mathrm{d}z}\begin{pmatrix} x \\ y \end{pmatrix} &= \tan\theta \left[\cos\left(\tan\theta \cdot \frac{z}{\rho} + \phi_i \right) \cos\phi_\mathrm{p} + \sin\left(\tan\theta \cdot \frac{z}{\rho} + \phi_i \right) \sin\phi_\mathrm{p} \right] \\ &= \tan\theta \cdot \cos\left(\tan\theta \cdot \frac{z}{\rho} + \phi_i - \phi_\mathrm{p} \right) < 0. \end{aligned} \tag{B.14}$$

We know that $\rho > 0$ and $\tan\theta > 0$ as $\theta \in (0, \frac{\pi}{2})$, so:

$$\cos\left(\tan\theta \cdot \frac{z}{\rho} + \phi_i - \phi_\mathrm{p} \right) < 0. \tag{B.15}$$

With $z = z_\mathrm{hit}$ from Eq. B.11:

$$\begin{aligned} \cos\left(\phi_\mathrm{p} - \phi_i + n\pi + (-1)^n \arcsin\left(\frac{a}{\rho} + \sin\left(\phi_i - \phi_\mathrm{p}\right) \right) + \phi_i - \phi_\mathrm{p} \right) &= \ldots \\ = (-1)^n \cos\left(\arcsin\left(\frac{a}{\rho} + \sin\left(\phi_i - \phi_\mathrm{p}\right) \right) \right). \end{aligned} \tag{B.16}$$

By the use of the identity:

$$\cos\left(\arcsin(x)\right) = \sqrt{1 - x^2}, \tag{B.17}$$

we obtain:

$$(-1)^n \cos\left(\arcsin\left(\frac{a}{\rho} + \sin\left(\phi_i - \phi_\mathrm{p}\right) \right) \right) = (-1)^n \sqrt{1 - \left(\frac{a}{\rho} + \sin\left(\phi_i - \phi_\mathrm{p}\right)^2 \right)} < 0, \tag{B.18}$$

which means that n is odd.

If $\phi_i = 0, \phi_p = \pi, n = 1$:

$$z_\mathrm{hit} = \frac{\rho}{\tan\theta} \left(2\pi - \arcsin\left(\frac{a}{\rho} \right) \right) = z_0 \left(1 - \frac{1}{2\pi} \arcsin\left(\frac{a}{\rho} \right) \right). \tag{B.19}$$

When $\rho \gg a$:

$$z_\mathrm{hit} \approx z_0 \left(1 - \frac{1}{2\pi} \frac{a}{\rho} \right). \tag{B.20}$$

B.1 Inverse problem for a finite detector

We want to find a transformation

$$\begin{pmatrix} E \\ z \end{pmatrix} \longrightarrow \begin{pmatrix} E_x \\ \theta_{\mathrm{cm}} \end{pmatrix}. \tag{B.21}$$

for a finite size detector. Recalling Eq. (2.18)

$$\begin{aligned} E &= \gamma q - \gamma\beta p \cos\theta_{cm}, \\ q &= \gamma E - \gamma\beta\alpha z. \end{aligned} \tag{B.22}$$

By combining Eq. (B.20) and Eq. (B.22) we obtain:

$$\alpha\beta\gamma z = (E\gamma - q)\Big(1 - \frac{1}{2\pi}\frac{a}{\rho}\Big). \tag{B.23}$$

The coupled solution is:

$$\begin{cases} E = \gamma q - \gamma\beta p \cos(\theta_{cm}), \\ \alpha\beta\gamma z = (\gamma E - q)\Big(1 - \frac{1}{2\pi}\frac{a}{\rho}\Big). \end{cases} \tag{B.24}$$

We know, that:

$$\begin{aligned} \rho &= \frac{p \sin\theta_{cm}}{cZB}, \qquad \text{and} \\ \sin\theta_{cm} &= \sqrt{1 - \cos^2\theta_{cm}}. \end{aligned} \tag{B.25}$$

The expression for $\cos\theta_{cm}$ can be obtained from Eq. (2.18). After solving that we obtain:

$$\Big(1 - \frac{1}{2\pi}\frac{a}{\rho}\Big) = 1 - \frac{\beta\gamma\alpha a}{\sqrt{2\gamma E q - E^2 - m^2\gamma^2 - p^2}}, \tag{B.26}$$

which leads to:

$$\boxed{\alpha\beta\gamma z = (\gamma E - q)\left(1 - \frac{\beta\gamma\alpha a}{\sqrt{2\gamma E q - E^2 - m^2\gamma^2 - p^2}}\right).} \tag{B.27}$$

When replacing

$$p \longrightarrow m\tan(x) \quad \text{with} \quad 0 < x < \frac{\pi}{2}, \tag{B.28}$$

Eq. (B.27) can be expressed as:

$$\alpha\beta\gamma z = (\gamma E - m\sec(x))\left(1 - \frac{\beta\gamma\alpha a}{\sqrt{2E\gamma m\sec(x) - E^2 - m^2\gamma^2 - m^2\tan^2(x)}}\right). \tag{B.29}$$

Let us use the following notation to give the above expression a shorter form:

$$\begin{gathered} E\gamma - m\sec(x) \longrightarrow K, \\ (E^2 - m^2)\gamma^2\beta^2 \longrightarrow H^2 > 0, \\ \alpha\beta\gamma z \longrightarrow Z, \\ \beta\gamma\alpha a \longrightarrow G > 0. \end{gathered} \tag{B.30}$$

Using the above notation, Eq. (B.29) becomes:

$$Z = K\left(1 - \frac{G}{\sqrt{H^2 - K^2}}\right), \tag{B.31}$$

which can be transformed into:

$$\begin{gathered} Z = H\sin\phi\left(1 - \frac{G}{H\cos\phi}\right), \\ \text{or} \\ Z = H\sin\phi - G\tan\phi, \end{gathered} \tag{B.32}$$

when replacing $K \longrightarrow H\sin\phi$, with $-\frac{\pi}{2} < \phi < \frac{\pi}{2}$.
When $a \to 0$, $G \to 0$, and the solution becomes:

$$Z = H\sin\phi = K = \gamma E - m\sec(x), \tag{B.33a}$$

$$\alpha\beta\gamma z = \gamma E - q, \tag{B.33b}$$

$$E = \frac{1}{\gamma}q + \alpha\beta z, \tag{B.33c}$$

which is consistent with a zero-size detector solution.

For a finite detector with $a \ll \rho$:

$$\frac{G}{\sqrt{H^2 - K^2}} = \frac{a}{2\pi\rho} < 1. \tag{B.34}$$

Therefore, the function

$$f(\phi) = H\sin\phi - G\tan\phi, \tag{B.35}$$

has shape as shown in Fig. B.3. When $\theta_{\rm cm}$ is small, there are multiple solutions for ϕ.

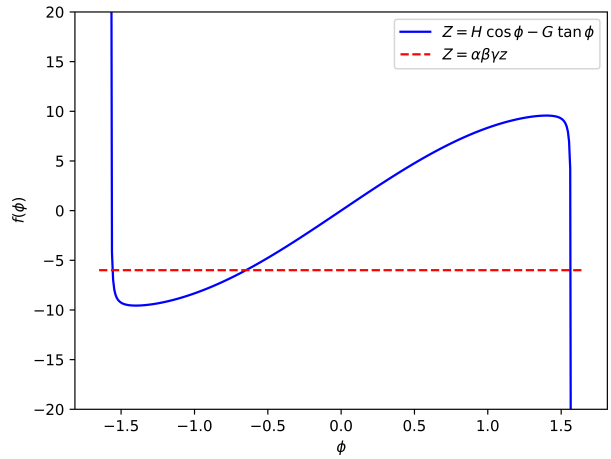

Figure B.3: $f(\phi) = H\cos\phi - G\tan\phi$ (blue solid line) and $f(\phi) = Z = \alpha\beta\gamma z$ (dashed red line). There are multi-solutions for ϕ when $\theta_{\rm cm}$ is small.

When $\theta_{\rm cm} \gg 0$, the derivative of the function is:

$$f'(\phi) = H\cos\phi - G\sec^2\phi > 0. \tag{B.36}$$

To find the solution, it is needed to use a numerical method, for example a Newton's method:

$$\phi_{i+1} = \phi_i - \frac{f(\phi_i)}{f'(\phi_i)} \tag{B.37}$$

Bibliography

[1] R. Bernas, E. Gradsztajn, H. Reeves, and E. Schatzman, "On the nucleosynthesis of lithium, beryllium, and boron", Annals of Physics **44**, 426–478 (1967).

[2] J. A. Johnson, "Populating the periodic table: Nucleosynthesis of the elements", Science **363**, 474–478 (2019), eprint: `https://www.science.org/doi/pdf/10.1126/science.aau9540`.

[3] E. M. Burbidge, G. R. Burbidge, W. A. Fowler, and F. Hoyle, "Synthesis of the Elements in Stars", Rev. Mod. Phys. **29**, 547–650 (1957).

[4] A. G. Cameron, "Stellar evolution, nuclear astrophysics, and nucleogenesis. Second edition", (1957).

[5] M Lugaro, S. W. Campbell, V D'Orazi, A. I. Karakas, D. A. Garcia-Hernandez, R. J. Stancliffe, G Tagliente, C Iliadis, and T Rauscher, "Current hot questions on the s process in AGB stars", Journal of Physics: Conference Series **665**, 012021 (2016).

[6] Cseh, B., Lugaro, M., D´Orazi, V., de Castro, D. B., Pereira, C. B., Karakas, A. I., Molnár, L., Plachy, E., Szabó, R., Pignatari, M., and Cristallo, S., "The s process in AGB stars as constrained by a large sample of barium stars", A&A **620**, A146 (2018).

[7] M. Lugaro, F. Herwig, J. C. Lattanzio, R. Gallino, and O. Straniero, "s-Process Nucleosynthesis in Asymptotic Giant Branch Stars: A Test for Stellar Evolution", The Astrophysical Journal **586**, 1305 (2003).

[8] F. Käppeler, R. Gallino, S. Bisterzo, and W. Aoki, "The *s* process: nuclear physics, stellar models, and observations", Rev. Mod. Phys. **83**, 157–193 (2011).

[9] D. Watson, C. Hansen, J. Selsing, A. Koch, D. Malesani, A. Andersen, J. Fynbo, A. Arcones, A. Bauswein, S. Covino, A. Grado, K. Heintz, L. Hunt, C. Kouveliotou, G. Leloudas, A. Levan, P. Mazzali, and E. Pian, "Identification of strontium in the merger of two neutron stars", Nature **574**, 497–500 (2019).

[10] B. P. Abbott et al., "GW170817: Observation of Gravitational Waves from a Binary Neutron Star Inspiral", Phys. Rev. Lett. **119**, 161101 (2017).

[11] C. Sneden and J. J. Cowan, "Genesis of the Heaviest Elements in the Milky Way Galaxy", Science **299**, 70–75 (2003), eprint: `https://www.science.org/doi/pdf/10.1126/science.1077506`.

[12] J. Winfield, W. Catford, and N. Orr, "Neutron transfer reactions with radioactive beams", Nuclear Instruments and Methods in Physics Research Section A: Accelerators, Spectrometers, Detectors and Associated Equipment **396**, 147–164 (1997).

[13] J. Lighthall, B. Back, S. Baker, S. Freeman, H. Y. Lee, B. Kay, S. Marley, K. Rehm, J. Rohrer, J. Schiffer, D. Shetty, A. Vann, J. Winkelbauer, and A. Wuosmaa, "Commissioning of the HELIOS spectrometer", Nuclear Instruments and Methods in Physics Research Section A: Accelerators, Spectrometers, Detectors and Associated Equipment **622**, 97–106 (2010).

[14] Tsz Leung (Ryan) Tang, Kinematics in HELIOS detector and particle detection, (accessed online 23.11.2023).

[15] J. C. Lighthall, "Commissioning of the Helical Orbit Spectrometer: A New Device for Measuring Nuclear Reactions in Inverse Kinematics", PhD thesis (Western Michigan University, 2011).

[16] A. Svärdström, private communication.

[17] A. Plompen, O. Cabellos, C. De Saint Jean, M. Fleming, A. Algora, M. Angelone, P. Archier, E. Bauge, O. Bersillon, A. Blokhin, F. Cantargi, A. Chebboubi, C. Diez, H. Duarte, E. Dupont, J. Dyrda, B. Erasmus, L. Fiorito, U. Fischer, D. Flammini, D. Foligno, M. Gilbert, J. Granada, W. Haeck, F. Hambsch, P. Helgesson, S. Hilaire, I. Hill, H. Mursin, R. Ichou, R. Jacqmin, B. Jansky, C. Jouanne, M. Kellett, D. Kim, H. Kim, I. Kodeli, A. Koning, A. Konobeyev, S. Kopecky, B. Kos, A. Krasa, L. Leal, N. Leclaire, P. Leconte, Y. Lee, H. Leeb, O. Litaize, M. Majerle, J. M. Damian, F. Michel-Sendis, R. Mills, B. Morillon, G. Noguere, M. Pecchia, S. Pelloni, P. Pereslavtsev, R. Perry, D. Rochman, R. Roehrmoser, P. Romain, P. Romojaro, D. Roubtsov, P. Sauvan, P. Schillebeeckx, K. Schmidt, O. Serot, S. Simakov, I. Sirakov, H. Sjöstrand, A. Stankovskiy, J. Sublet, P. Tamagno, A. Trkov, S. Van Den Marck, F. Velarde, R. Villari, K. Yokoyama, and G. Zerovnik, "The Joint Evaluated Fission and Fusion Nuclear Data Library, JEFF-3.3", European Physical Journal A **56**, 181 (2020).

[18] D. Brown, M. Chadwick, R. Capote, A. Kahler, A. Trkov, M. Herman, A. Sonzogni, Y. Danon, A. Carlson, M. Dunn, D. Smith, G. Hale, G. Arbanas, R. Arcilla, C. Bates, B. Beck, B. Becker, F. Brown, R. Casperson, J. Conlin, D. Cullen, M.-A. Descalle, R. Firestone, T. Gaines, K. Guber, A.

Hawari, J. Holmes, T. Johnson, T. Kawano, B. Kiedrowski, A. Koning, S. Kopecky, L. Leal, J. Lestone, C. Lubitz, J. Márquez Damián, C. Mattoon, E. McCutchan, S. Mughabghab, P. Navratil, D. Neudecker, G. Nobre, G. Noguere, M. Paris, M. Pigni, A. Plompen, B. Pritychenko, V. Pronyaev, D. Roubtsov, D. Rochman, P. Romano, P. Schillebeeckx, S. Simakov, M. Sin, I. Sirakov, B. Sleaford, V. Sobes, E. Soukhovitskii, I. Stetcu, P. Talou, I. Thompson, S. van der Marck, L. Welser-Sherrill, D. Wiarda, M. White, J. Wormald, R. Wright, M. Zerkle, G. Žerovnik, and Y. Zhu, "ENDF/B-VIII.0: The 8th Major Release of the Nuclear Reaction Data Library with CIELO-project Cross Sections, New Standards and Thermal Scattering Data", Nuclear Data Sheets **148**, Special Issue on Nuclear Reaction Data, 1–142 (2018).

[19] K. Shibata, O. Iwamoto, T. Nakagawa, N. Iwamoto, A. Ichihara, S. Kunieda, S. Chiba, K. Furutaka, N. Otuka, T. Ohsawa, T. Murata, H. Matsunobu, A. Zukeran, S. Kamada, and J. ichi KATAKURA, "JENDL-4.0: A New Library for Nuclear Science and Engineering", Journal of Nuclear Science and Technology **48**, 1–30 (2011).

[20] S. Bjørnholm and J. E. Lynn, "The double-humped fission barrier", Rev. Mod. Phys. **52**, 725–931 (1980).

[21] D. Ramos, M. Caamaño, A. Lemasson, M. Rejmund, L. Audouin, H. Álvarez-Pol, J. D. Frankland, B. Fernández-Domínguez, E. Galiana-Baldó, J. Piot, D. Ackermann, S. Biswas, E. Clement, D. Durand, F. Farget, M. O. Fregeau, D. Galaviz, A. Heinz, A. I. Henriques, B. Jacquot, B. Jurado, Y. H. Kim, P. Morfouace, D. Ralet, T. Roger, C. Schmitt, P. Teubig, and I. Tsekhanovich, "First Direct Measurement of Isotopic Fission-Fragment Yields of ^{239}U", Phys. Rev. Lett. **123**, 092503 (2019).

[22] J. N. Wilson, M. Lebois, L. Qi, P. Amador-Celdran, D. Bleuel, J. A. Briz, R. Carroll, W. Catford, H. De Witte, D. T. Doherty, R. Eloirdi, G. Georgiev, A. Gottardo, A. Goasduff, K. Hadyńska-Klęk, K. Hauschild, H. Hess, V. Ingeberg, T. Konstantinopoulos, J. Ljungvall, A. Lopez-Martens, G. Lorusso, R. Lozeva, R. Lutter, P. Marini, I. Matea, T. Materna, L. Mathieu, A. Oberstedt, S. Oberstedt, S. Panebianco, Z. Podolyák, A. Porta, P. H. Regan, P. Reiter, K. Rezynkina, S. J. Rose, E. Sahin, M. Seidlitz, O. Serot, R. Shearman, B. Siebeck, S. Siem, A. G. Smith, G. M. Tveten, D. Verney, N. Warr, F. Zeiser, and M. Zielinska, "Anomalies in the Charge Yields of Fission Fragments from the ^{238}U(n, f) Reaction", Phys. Rev. Lett. **118**, 222501 (2017).

[23] A. Wuosmaa, J. Schiffer, B. Back, C. Lister, and K. Rehm, "A solenoidal spectrometer for reactions in inverse kinematics", NIM A **580**, 1290–1300 (2007).

[24] S. A. Bennett, K. Garrett, D. K. Sharp, S. J. Freeman, A. G. Smith, T. J. Wright, B. P. Kay, T. L. Tang, I. A. Tolstukhin, Y. Ayyad, J. Chen, P. J. Davies, A. Dolan, L. P. Gaffney, A. Heinz, C. R. Hoffman, C. Müller-Gatermann, R. D. Page, and G. L. Wilson, "Direct Determination of Fission-Barrier Heights Using Light-Ion Transfer in Inverse Kinematics", Phys. Rev. Lett. **130**, 202501 (2023).

[25] S. Singh and B. Singh, "Nuclear Data Sheets for A = 224", Nuclear Data Sheets **130**, 127–182 (2015).

[26] E. Browne and J. Tuli, "Nuclear Data Sheets for A = 220", Nuclear Data Sheets **112**, 1115–1161 (2011).

[27] M. J. Martin, "Nuclear Data Sheets for A = 208", Nuclear Data Sheets **108**, 1583–1806 (2007).

[28] S.-C. Wu, "Nuclear Data Sheets for A = 216", Nuclear Data Sheets **108**, 1057–1092 (2007).

[29] K. Auranen and E. McCutchan, "Nuclear Data Sheets for A=212", Nuclear Data Sheets **168**, 117–267 (2020).

[30] R. Brun and F. Rademakers, "ROOT: An object oriented data analysis framework", Nucl. Instrum. Meth. A **389**, edited by M. Werlen and D. Perret-Gallix, 81–86 (1997).

[31] Y. Blumenfeld et al., "Facilities and methods for radioactive ion beam production", Phys. Scr. **2013**, 014023.

[32] W. Weterings, C. Bracco, L. O. Jorat, M. Meddahi, R. Noulibos, and P. Van Trappen, "The new injection region of the CERN PS Booster", in 10th International Particle Accelerator Conference (2019), WEPMP039.

[33] F. Landua, "The CERN accelerator complex layout in 2022. Complexe des accélérateurs du CERN en janvier 2022", General Photo (2022).

[34] R. Catherall et al., J. Phys. G: Nucl. Part. Phys. **44**, 094002 (2017).

[35] F. Wenander, "Charge breeding of radioactive ions with EBIS and EBIT", Journal of Instrumentation **5**, C10004 (2010).

[36] F. Wenander et al., REXEBIS, the electron beam ion source for the REX-ISOLDE project: Design and simulations, CERN OPEN-2000-320 (2000).

[37] M. J. G. Borge and K. Riisager, "HIE-ISOLDE, the project and the physics opportunities", Eur. Phys. J. A **52**, 10.1140/epja/i2016-16334-4 (2016).

[38] Y. Kadi, M. A. Fraser and A.Papageorgiou-Koufidou, "HIE-ISOLDE: Technical Design Report for the Energy Upgrade", CERN Yellow Reports: Monographs, Vol. 1/2018, CERN-2018-002-M(CERN, Geneva, 2018).

[39] G. Battistoni, F. Cerutti, A. Fassò, A. Ferrari, S. Muraro, J. Ranft, S. Roesler, and P. R. Sala, "The FLUKA code: description and benchmarking", AIP Conference Proceedings **896**, 31–49 (2007), eprint: `https://pubs.aip.org/aip/acp/article-pdf/896/1/31/11572161/31\_1\_online.pdf`.

[40] R. Wolf, F. Wienholtz, D. Atanasov, D. Beck, K. Blaum, C. Borgmann, F. Herfurth, M. Kowalska, S. Kreim, Y. A. Litvinov, D. Lunney, V. Manea, D. Neidherr, M. Rosenbusch, L. Schweikhard, J. Stanja, and K. Zuber, "ISOLTRAP's multi-reflection time-of-flight mass separator/spectrometer", International Journal of Mass Spectrometry **349-350**, 100 years of Mass Spectrometry, 123–133 (2013).

[41] M. Au, private communication.

[42] "Search for β-delayed fission of the heavy neutron-rich isotope 230Ac", The European Physical Journal A - Hadrons and Nuclei **10**, 1–3 (2001).

[43] M. Thoennessen and G. F. Bertsch, "Threshold for dissipative fission", Phys. Rev. Lett. **71**, 4303–4306 (1993).

[44] S. Wang, INDC(CPR)-056/L, p.15 (2001).

[45] E.-M. Eckert, A. Kühmichel, J. Pochodzalla, K. D. Hildenbrand, U. Lynen, W. F. J. Müller, H. J. Rabe, H. Sann, H. Stelzer, W. Trautmann, R. Trockel, R. Wada, C. Cerruti, P. Lhénoret, R. Lucas, C. Mazur, C. Ng, M. Ribrag, E. Tomasi, A. Demeyer, and D. Guinet, "Transient times of fission in ^{40}Ar+^{232}Th peripheral collisions", Phys. Rev. Lett. **64**, 2483–2486 (1990).

[46] K.-H. Schmidt, B. Jurado, C. Amouroux, and C. Schmitt, "General Description of Fission Observables: GEF Model Code", Nuclear Data Sheets **131**, Special Issue on Nuclear Reaction Data, 107–221 (2016).

[47] L. Ghys, A. N. Andreyev, S. Antalic, M. Huyse, and P. Van Duppen, "Empirical description of β-delayed fission partial half-lives", Phys. Rev. C **91**, 044314 (2015).

[48] J. N. Wilson et al., "Angular momentum generation in nuclear fission", Nature (London) **590**, 566 –570 (2021).

[49] H. T. Törnqvist, private communication.

[50] M. V. Managlia, private communication.

[51] O. Tarasov and D. Bazin, "Lise++: radioactive beam production with in-flight separators", Nuclear Instruments and Methods in Physics Research Section B: Beam Interactions with Materials and Atoms **266**, Proceedings of the XVth International Conference on Electromagnetic Isotope Separators and Techniques Related to their Applications, 4657–4664 (2008).

[52] O. Poleshchuk, R. Raabe, S. Ceruti, A. Ceulemans, H. De Witte, T. Marchi, A. Mentana, J. Refsgaard, and J. Yang, "The SpecMAT active target", Nuclear Instruments and Methods in Physics Research Section A: Accelerators, Spectrometers, Detectors and Associated Equipment **1015**, 165765 (2021).

[53] S. Bennett, D. Sharp, and T. Wright, *Probing the fission and radiative decay of the* ^{235}*U+n system using (d,pf) and (d,p*γ*) reactions*, tech. rep. (CERN, Geneva, 2023).

[54] G. Henning, T. L. Khoo, A. Lopez-Martens, D. Seweryniak, M. Alcorta, M. Asai, B. B. Back, P. F. Bertone, D. Boilley, M. P. Carpenter, C. J. Chiara, P. Chowdhury, B. Gall, P. T. Greenlees, G. Gürdal, K. Hauschild, A. Heinz, C. R. Hoffman, R. V. F. Janssens, A. V. Karpov, B. P. Kay, F. G. Kondev, S. Lakshmi, T. Lauritsen, C. J. Lister, E. A. McCutchan, C. Nair, J. Piot, D. Potterveld, P. Reiter, A. M. Rogers, N. Rowley, and S. Zhu, "Fission Barrier of Superheavy Nuclei and Persistence of Shell Effects at High Spin: Cases of ^{254}No and ^{220}Th", Phys. Rev. Lett. **113**, 262505 (2014).